

Sensitivity of Nozzle Guide Vane Flow Capacity to Geometric Changes

Tom Franklyn Gammage

September 2021

Thanks

Abstract

Contents

List of Figures	5
List of Tables	8
1 Introduction	10
1.1 Motivation	10
1.2 Flow capacity: background, definition, and derivation	12
1.3 Research structure	14
1.4 Summary of findings	15
2 Geometric throat area	16
2.1 Nozzle guide vane capacity uncertainty in 2 dimensions	18
2.1.1 Geometry, mesh, and boundary conditions	18
2.1.2 Effect on 2D capacity	25
2.2 Comparison of 2D capacity predictions with 3D data	32
2.2.1 Effect on 2D capacity versus 3D capacity	32
2.3 Chapter conclusions	34
3 Trailing edge	35
3.1 Definitions of loss for trailing edge performance evaluation	37
3.2 Effects of suction-side trailing edge shape uncertainty	40
3.2.1 Geometry, mesh, and boundary conditions	40
3.2.2 Effect on capacity	42
3.2.3 Effect on performance	48

3.3	Effects of pressure-side trailing edge sizing	51
3.3.1	Geometry, mesh, and boundary conditions	52
3.3.2	Effect on capacity	53
3.3.3	Effect on performance	59
3.4	Chapter conclusions	62
4	Film cooling	63
4.1	Sensitivity of capacity to cooling holes on the leading suction side	63
4.1.1	Geometry, mesh, and boundary conditions	64
4.1.2	Effect on capacity	67
4.1.3	Effect on performance	73
Bibliography		74
Bibliography		75

List of Figures

1.1	<i>p-v</i> and <i>T-s</i> plots of the Brayton thermodynamic cycle	10
2.1	Considerations for defining minimum area	17
2.2	Creation of 2D mid-span approximation of NGV geometry	19
2.3	Computational domain and boundaries	20
2.4	Mesh for Trent 900 throat width variation study	24
2.5	Details of mesh for Trent 900 throat width variation study	25
2.6	Contours of Mach number for whole solution on vane KSZ03 at $\frac{p_{01}}{p_2} = 3.33$	26
2.7	Contours of Mach number for solution near throat on vane KSZ03 at $\frac{p_{01}}{p_2} = 3.33$	27
2.8	2D capacity trends for 6 Trent 900 NGVs	28
2.9	Sonic lines for 6 Trent 900 NGVs at $\frac{p_{01}}{p_2} = 3.33$	29
2.10	2D NGV capacity percentage delta as a function of 2D throat width for 6 NGVs at $\frac{p_{01}}{p_2} = 1.79$ (design)	30
2.11	2D NGV capacity percentage delta as a function of 2D A_{eff} for 6 NGVs at $\frac{p_{01}}{p_2} = 1.79$ (design)	31
2.12	3D capacity trends for 6 Trent 900 NGVs	32
2.13	3D NGV capacity percentage delta as a function of 3D throat area for 6 NGVs at $\frac{p_{01}}{p_2} = 1.79$ (design)	33
3.1	Main features of Trent nozzle guide vane trailing edge	36
3.2	Geometry processing scheme for cutbacks to the end-edge of a Trent 900 NGV	41
3.3	Example of mesh for cutbacks to the end-edge of a Trent 900 NGV	42
3.4	Effects of small cutbacks on sonic line shape for Trent 900 end-edge erosion study at $\frac{p_{01}}{p_2} = 3.33$	43

3.5 Effects of large cutbacks on sonic line shape for Trent 900 end-edge erosion study at $\frac{p_{01}}{p_2} = 3.33$	44
3.6 Effects of full range of cutbacks on sonic line shape for Trent 900 end-edge erosion study, labelled by 10% of end-edge removed	45
3.7 2D capacity percentage delta as a function of end-edge cutback amount for 3 pressure ratios	46
3.8 Contours of Mach number in the wake region of the Trent 900 end-edge erosion study at $\frac{p_{01}}{p_2} = 1.79$ (design)	47
3.9 2D capacity trends for various end-edge cutback amounts	48
3.10 NGV turning angle delta as a function of end-edge cutback amount at $\frac{p_{01}}{p_2} = 1.79$. . .	49
3.11 Outlet plane turning angle surveys for various end-edge cutback amounts at $\frac{p_{01}}{p_2} = 1.79$	49
3.12 Loss as a function of end-edge cutback amount at $\frac{p_{01}}{p_2} = 1.79$	50
3.13 Loss delta as a function of capacity delta for end-edge cutbacks at $\frac{p_{01}}{p_2} = 1.79$	51
3.14 Geometry processing scheme for cutbacks to the pressure side of a Trent 900 NGV . .	52
3.15 Examples of meshes for cutbacks to the pressure side of a Trent 900 NGV	53
3.16 Effects of cutbacks on sonic line shape for Trent 900 pressure-side cutback study at $\frac{p_{01}}{p_2} = 3.33$	54
3.17 NGV geometric throat width as a function of cutback amount	55
3.18 Effects of full range of cutbacks on sonic line shape for Trent 900 pressure-side cutbacks study, labelled by % of cutback	55
3.19 2D capacity percentage delta as a function of pressure-side cutback amount for 3 pressure ratios	56
3.20 Effects of cutbacks on trailing edge aerodynamics for Trent 900 pressure-side cutback study at $\frac{p_{01}}{p_2} = 1.79$ (design)	57
3.21 2D capacity trends for various pressure-side cutback amounts	58
3.22 NGV turning angle delta as a function of pressure-side cutback amount at $\frac{p_{01}}{p_2} = 1.79$	59
3.23 Outlet plane turning angle surveys for various pressure-side cutback amounts at $\frac{p_{01}}{p_2} = 1.79$	60
3.24 Loss as a function of pressure-side cutback amount at $\frac{p_{01}}{p_2} = 1.79$	61
3.25 Loss delta as a function of capacity delta for pressure-side cutbacks at PR = 1.79 . . .	61
4.1 Computational domain and boundaries for a film cooling hole and plenum	64
4.2 Range of locations for a single suction-side film cooling hole on a Trent XWB NGV . .	66

4.3	Details of mesh for XWB single cooling hole study	67
4.4	Effects of cooling hole location on Mach contours for Trent XWB film cooling study at $\frac{p_{01}}{p_2} = 1.65$	68
4.5	Effects of cooling hole location on Mach contours for Trent XWB film cooling study at $\frac{p_{01}}{p_2} = 1.65$	69
4.6	Total capacity percentage delta as a function of single cooling hole position	70
4.7	Total capacity percentage delta as a function of surface isentropic Mach number . . .	71
4.8	Coolant capacity percentage delta as a function of single cooling hole position	72
4.9	Coolant capacity percentage delta as a function of single cooling hole position	73
4.10	Loss as a function of single cooling hole position	73

List of Tables

2.1	Boundary conditions at design pressure ratio for multi-vane capacity study	20
2.2	Values for calculating NGV Reynolds number	21
2.3	Throat widths of 6 Trent 900 NGVs	29
2.4	Throat areas of 6 Trent 900 NGVs	33
3.1	Boundary conditions for end-edge shape uncertainty study	40
4.1	Boundary conditions for suction-side cooling hole position study	65

Nomenclature

Romans

Greeks

Acronyms and Abbreviations

Subscripts

Chapter 1

Introduction

Jet engines are not perfect. Contemporary analysis does not provide a complete understanding of the phenomena by which turbomachinery flows differ from 1-dimensional compressible flow. Contemporary engineering does not provide a realisation of the best performing engine that could be built, but is instead limited by the capabilities of materials and manufacturing. It will be shown that improved analytical understanding and improved engine performance both depend on predicting the engine core mass flow rate as accurately as possible. This thesis will analyse the high-pressure turbine nozzle guide vanes (NGVs), this being the component that limits the engine core mass flow rate. Further analyses will examine the aerodynamic performance of this component in terms of its ability to impart the correct whirl angle to the post-combustor flow with minimal loss, so as to most efficiently deliver the flow to the high pressure turbine and beyond.

1.1 Motivation

The requirement for an accurate core mass flow rate prediction is illustrated by consideration of the Brayton thermodynamic cycle, which is plotted in Figure 1.1.

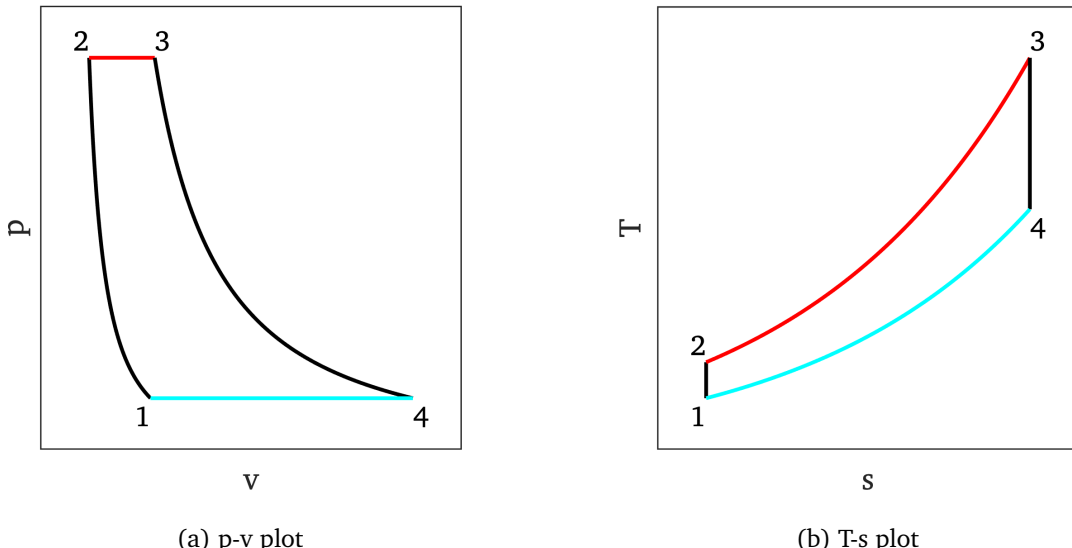


Figure 1.1: p - v and T - s plots of the Brayton thermodynamic cycle

Basic analysis of the Brayton cycle shows that its thermal efficiency is equal to

$$\eta_{th} = 1 - \left(\frac{p_1}{p_2} \right)^{\frac{\gamma-1}{\gamma}} \quad (1.1)$$

For maximum thermal efficiency, it is thus desirable to maximise the pressure increase produced by the engine's compressor, which is responsible for the process of isentropic compression between stations 1 and 2. The compression ratio is limited in practice by the pressure increase that is achievable by contemporary compressors, which must balance the goal with the avoidance of stall, the need for a wide range of operating conditions, and the avoidance of excess complexity from adding additional spools. Cruise-condition compression ratio is thus a design specification which sets the value of p_2 .

The engine's combustor is responsible for the process of isobaric heat addition between stations 2 and 3. The rate of heat addition to the flow is given by

$$Q_{23} = \dot{m}c_p(T_3 - T_2) \quad (1.2)$$

where \dot{m} is the mass flow rate through the combustor. For the purpose of illustration, the influences of bleed and cooling air mass flow rate are not considered, and \dot{m} is taken to be the mass flow rate through the engine compressor, combustor, nozzle guide vanes, and turbine. c_p is the specific heat of air at constant pressure and T_2 is derived from the compressor inlet temperature T_1 via isentropic compression as

$$T_2 = T_1 \left(\frac{p_2}{p_1} \right)^{\frac{\gamma-1}{\gamma}} \quad (1.3)$$

combining to express the heat added as

$$Q_{23} = \dot{m}c_p \left[T_3 - T_1 \left(\frac{p_2}{p_1} \right)^{\frac{\gamma-1}{\gamma}} \right] \quad (1.4)$$

For maximum power, it is desirable to maximise the heat added to the flow, which would result in an increase in T_3 . A technological limitation is once again presented: the maximum T_3 is limited by the avoidance of overheating the post-combustor nozzle guide vanes, for which heat management is of prime concern to the field. T_3 is thus a design specification.

Heat addition is well controlled for in contemporary lean-burn engines, where it may be modelled by the relationship

$$Q_{23} = \eta_h H_{LV} \dot{m}_f \quad (1.5)$$

where \dot{m}_f is the fuel mass flow rate, H_{LV} is the lower heating value of jet fuel and η_h is a constant to account for inefficiencies of heat addition beyond the scope of the present illustration. The above equations combine to show that the required fuel mass flow rate may be modelled by the expression

$$\frac{\dot{m}_f}{\dot{m}} = \frac{c_p}{\eta_h H_{LV}} \left(T_3 - T_1 r_p^{\frac{\gamma-1}{\gamma}} \right) \quad (1.6)$$

where r_p is the compression ratio, $\frac{p_2}{p_1}$. It is shown that the core mass flow rate, \dot{m} , must be accurately predicted if the engine is to be accurately maintained at the optimal operating conditions allowed by its construction. r_p and T_3 are known design specifications, T_1 is a measurable ambient condition, and all other terms are approximately constant.

The design of any jet engine depends on the assumption that accurate prediction of \dot{m} is possible. It has been shown that this is directly tied to the performance and operational margins of the upstream engine components. Predictability of \dot{m} also affects the design of every downstream turbine stage. If

it differs from its expected value due to a poor prediction, all subsequent turbine stages will be sized for an incorrect mass flow rate. The resulting errors in flow velocity and pressure will compound with each additional stage, leading to increasingly incorrect specification of turbine sizes and turning angles.

Andrea Guiffre' and Matteo Pini [1] performed numerical analysis to discuss scaleable guidelines for turbine stage design, validating their model using high-fidelity CFD. Correct stage matching was found to be highly dependent on matching the *volumetric flow ratio*, defined by the authors as a stage's total-to-static density ratio. To accurately quantify this parameter within the analytical and computational methods discussed in this thesis, mass flow rate would need to be predicted correctly.

A strong understanding of NGV mass flow rate predictability should allow engine-makers to pre-empt geometric changes that happen to NGVs during service, such as erosion and cooling hole blockage. It should also account for geometric uncertainties arising from the manufacturing process. While this study advocates for improved accuracy of capacity predictions, emphasis is placed on how these predictions are limited by the unpredictability of real-world manufacture and service.

Section 1.2 will outline the analysis involved in parameterising and predicting mass flow rate. The section will also present the alternative metric of *flow capacity* as a more useful way of characterising mass flow rate independently of the NGV upstream total pressure and temperature. Defining a purely geometric mass flow rate capacity allows for experimental testing of NGVs without recreating the extreme boundary conditions to which real NGVs are exposed. Setting the correct pressure ratio is sufficient, as the subsequent derivation will show. This expedites the testing of different NGV geometries' effects on mass flow rate.

1.2 Flow capacity: background, definition, and derivation

The capacity of an internal combustion engine is an intuitive concept. It is simple to derive from the engine's geometry, it has tangible units of volume, and it provides an heuristic for the engine's size, performance, and air mass flow rate. The design of turbomachinery invites an analogous concept to that of IC engine capacity, but a definition is not so obvious. Mass flow rate through an engine's nozzle guide vane is a function of the NGV's geometry and of its boundary conditions. If the mass flow rate can be quantified in a way which mitigates the boundary conditions, then the effects of an NGV's geometry on its mass flow rate may be isolated. A particular NGV will thus have a mass flow rate capacity, just as a particular IC cylinder has a volumetric capacity.

In 1 dimension, an engine nozzle may be modelled as a compressible flow from an upstream reservoir of total pressure p_0 , accelerating to velocity v and density ρ through a nozzle of cross-sectional area A . Mass flow rate through the nozzle is thus

$$\dot{m} = \rho A v \quad (1.7)$$

where density may be expressed as a function of *pressure ratio*, the ratio of the nozzle pressure to the total pressure

$$\rho = \frac{p_0}{RT_0} \left(\frac{p}{p_0} \right)^{\frac{1}{\gamma}} \quad (1.8)$$

and velocity is given by the compressible form of Bernoulli's equation as

$$v = \sqrt{2 \left(\frac{\gamma}{\gamma - 1} \right) \left[\frac{p_0}{\rho_0} - \frac{p}{\rho} \right]} \quad (1.9)$$

The above equations combine to express mass flow rate through the nozzle as

$$\dot{m} = A \frac{p_0}{RT_0} \left(\frac{p}{p_0} \right)^{\frac{1}{\gamma}} \sqrt{2 \left(\frac{\gamma}{\gamma-1} \right) \left[\frac{p_0}{\left(\frac{p_0}{RT_0} \right)} - \frac{p}{\left(\frac{p_0}{RT_0} \right) \left(\frac{p}{p_0} \right)^{\frac{1}{\gamma}}} \right]} \quad (1.10)$$

which simplifies to

$$\dot{m} = A \frac{p_0}{RT_0} \left(\frac{p}{p_0} \right)^{\frac{1}{\gamma}} \sqrt{2 \left(\frac{\gamma}{\gamma-1} \right) \left[RT_0 - RT_0 \left(\frac{p}{p_0} \right)^{\frac{\gamma-1}{\gamma}} \right]} \quad (1.11)$$

$$\dot{m} = \frac{p_0}{\sqrt{T_0}} A \sqrt{\frac{\gamma}{R}} \left(\frac{p}{p_0} \right)^{\frac{1}{\gamma}} \sqrt{\left(\frac{2}{\gamma-1} \right) \left[1 - \left(\frac{p}{p_0} \right)^{\frac{\gamma-1}{\gamma}} \right]} \quad (1.12)$$

Using \dot{m} from Equation 1.12, capacity is defined as

$$\Gamma = \frac{\sqrt{T_0}}{p_0} \dot{m} \quad (1.13)$$

This provides an expression of mass flow rate independent of upstream total pressure p_0 and upstream total temperature T_0 . The expression is purely a function of throat area A and pressure ratio $\frac{p}{p_0}$:

$$\Gamma = A \sqrt{\frac{\gamma}{R}} \left(\frac{p}{p_0} \right)^{\frac{1}{\gamma}} \sqrt{\left(\frac{2}{\gamma-1} \right) \left[1 - \left(\frac{p}{p_0} \right)^{\frac{\gamma-1}{\gamma}} \right]} \quad (1.14)$$

A scale constant σ is defined as

$$\sigma = \sqrt{\frac{2\gamma}{R(\gamma-1)}} \quad (1.15)$$

for a compact expression of capacity as a function of throat area A and pressure ratio r :

$$\Gamma(A, r) = \sigma A \sqrt{r^{\frac{2}{\gamma}} \left(1 - r^{\frac{\gamma-1}{\gamma}} \right)} \quad (1.16)$$

This expression has its maximum value at the critical pressure ratio

$$r_c = \left(\frac{\gamma+1}{2} \right)^{\frac{\gamma}{1-\gamma}} \quad (1.17)$$

At lower ratios, the nozzle is choked and mass flow rate cannot increase further. Choked capacity is given by

$$\Gamma_c(A) = \sqrt{\frac{2\gamma}{R(\gamma-1)}} A \sqrt{\left(\frac{\gamma+1}{2} \right)^{\frac{2}{1-\gamma}} \left[1 - \left(\frac{\gamma+1}{2} \right)^{-1} \right]} \quad (1.18)$$

which simplifies to

$$\Gamma_c(A) = \sqrt{\frac{2\gamma}{R(\gamma-1)}} A \sqrt{\left(\frac{\gamma+1}{2} \right)^{\frac{2}{1-\gamma}} \left[\frac{\gamma+1}{\gamma+1} - \left(\frac{2}{\gamma+1} \right) \right]} \quad (1.19)$$

$$\Gamma_c(A) = A \sqrt{\frac{2\gamma}{R}} (\gamma+1)^{\frac{2}{1-\gamma}} \frac{1}{\gamma+1} \left(\frac{1}{2} \right)^{\frac{2}{1-\gamma}} \quad (1.20)$$

$$\Gamma_c(A) = A \sqrt{\frac{\gamma}{R}} \left(\frac{\gamma+1}{2} \right)^{\frac{1+\gamma}{2(1-\gamma)}} \quad (1.21)$$

It is shown that the capacity of one-dimensional nozzle flow is a function of only the flow's minimum area, provided the flow is choked and the ratio of specific heats is assumed constant.

Section 1.3 will introduce the structure of the following chapters, which are to analyse the capacity of 2-dimensional and 3-dimensional nozzle flows, presenting and discussing analytical techniques for applying the 1D capacity equation to 2D and 3D data. In such cases, capacity will be defined by equation 1.13.

1.3 Research structure

The present study seeks to categorise and examine the ways in which nozzle guide vane flow departs from 1-dimensional compressible flow. These departures are numerous and diverse. The study's scope is to include 2 categories of phenomena: difficulties in predicting the mass flow rate through real nozzle guide vanes, and difficulties in quantifying and modelling the loss incurred by various practical solutions to the need for NGV coolant flow.

Although NGV flow capacity is arguably to be maximised in pursuit of greater power, and loss is certainly to be minimised in pursuit of greater efficiency, it is practical to divide efforts according to the areas of NGV engineering where limitations are present. The present study has identified 3 such areas.

- NGV casting processes causing variations in overall shape and throat area, limiting the predictability of flow capacity.
- Trailing edge machining processes causing variations in trailing edge shape, resulting in complex variations in the flow field near the downstream extremity of the trailing edge, with corresponding variations in flow capacity.
- Sensitivity of flow capacity to the addition of extra film cooling holes on the NGV leading edge suction side, including sensitivity to their exact location.

NGVs are cast to high precision. Chapter 2 will present the variations that nonetheless exist among sets of vanes that are intended to be identical. These variations are shown to affect the NGVs' geometric throat area. The chapter discusses the challenges inherent in finding a definition of throat area that usefully predicts the flow capacity of an NGV. The effects of 2-dimensional flow phenomena and geometric variations are presented as confounding factors when considering 2D nozzle flow as opposed to 1D. Further complexity is shown to arise when extending analyses to 3D, where 3D CFD data gathered by Rolls-Royce plc are compared to 2D CFD data from the present study.

Chapter 3 will discuss the other way in which NGV manufacturing introduces geometric variations that reduce capacity predictability, namely the machining of the trailing edge shape. The machining is designed to optimise the trailing edge's aerodynamics, and not necessarily to minimise variations in its shape. The chapter presents 2D CFD analyses of the effects of variable trailing edge cutback sizing on the 2D flow field and resulting flow capacity of the NGV. To address the variability of contemporary trailing edge designs and to examine the possibility of thicker trailing edges in the event of novel manufacturing methods, the chapter presents 2D CFD analyses of a design without a

cutback. This design's loss performance is analysed, informed by a review of various definitions of loss from the literature, where a lack of consensus on a loss definition is demonstrated.

Chapter 4 will analyse the effects of film coolant injection location on both flow capacity and loss. The chapter discusses the possible requirement for an additional suction-side film cooling hole row to be added to NGVs. Given the variability inherent in the process of drilling film cooling holes, justification is given for a 2D CFD study of the effects of hole location on flow capacity and loss, analogous to the variable trailing edge study of Chapter 3. A correlation between hole location and flow capacity is analysed, as is the hole location's effect on loss. The chapter also presents a quasi-3D CFD study to demonstrate that 2D CFD (which amounts to a cooling slot) does not accurately model the discharge and mixing phenomena of a row of circular holes.

Literature review will not be the subject of its own chapter. Literature will be reviewed throughout the thesis whenever relevant to the topic under discussion.

1.4 Summary of findings

Write this after you've got the findings.

Chapter 2

Geometric throat area

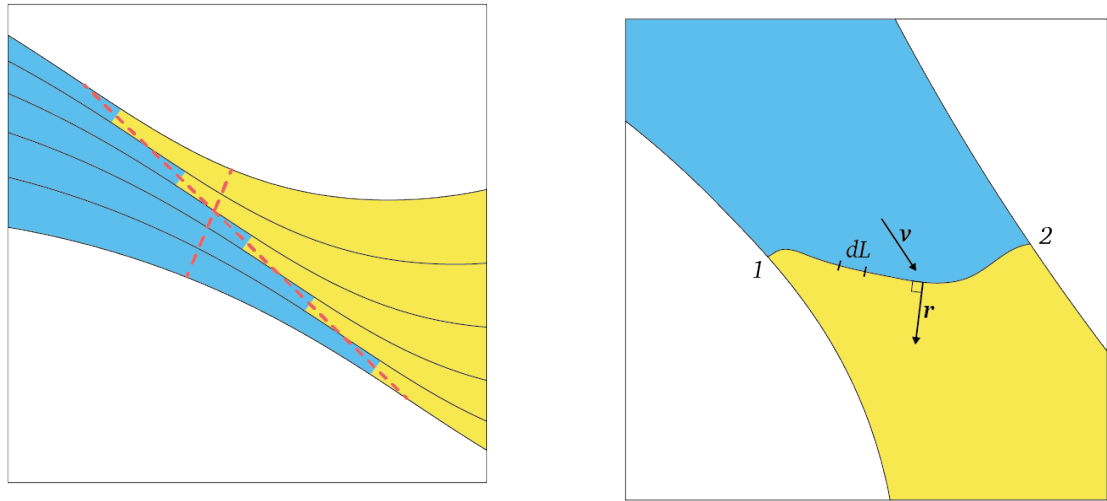
A 1-dimensional supersonic nozzle is equivalent to a single streamline of variable cross-sectional area. It is possible to solve for the flow conditions throughout the nozzle, provided area is specified as a function of position along the nozzle. The mass flow rate capacity is a function of only the flow's minimum area, as in equation 1.21.

A 2-dimensional fully choked nozzle may be modelled as a group of adjacent streamlines, each of which may have dissimilar area functions. The streamlines' minimum areas may not correspond to a straight line across the narrowest part of the nozzle. This is illustrated in Figure 2.1a by supposing the division of a 2-dimensional flow into a finite number of streams of finite width. Each stream has an individual point of minimum width where sonic conditions exist, shown as the transition between subsonic flow in blue and supersonic flow in yellow. These sonic points are distributed on a line distinct from the overall passage line of minimum width. The resulting minimum area line is shown in red along with the geometric minimum area line, to illustrate their disparity.

If this concept is extended to infinitesimal streamlines (and the flow is isentropic) each streamline will experience sonic conditions at its point of minimum area, coalescing to form the 2-dimensional sonic line. The effective throat area of a 2-dimensional nozzle is thus the sum of its streamlines' throat areas. This is distinct from the sonic line length, and may be expressed by the integral

$$A_{eff} = \int_1^2 \hat{v} \cdot \hat{r} dL \quad (2.1)$$

where \hat{v} is the unit vector of local flow velocity, \hat{r} is the unit vector perpendicular to the local sonic line, and the integral is performed on the scalar infinitesimal dL over the length of the sonic line, as illustrated in Figure 2.1b.



(a) Different minimum area points of dissimilar streams

(b) Integral for 2D nozzle equivalent throat area

Figure 2.1: Considerations for defining minimum area

In the case of 1-dimensional nozzle flow, Equation 2.1 collapses to the value of the throat area. In the case of 2D flow through an arbitrarily shaped nozzle such as a gas turbine nozzle guide vane, the integral describes the infinitesimal sum of the areas encountered by each streamline at the point of sonic conditions. It is proposed as a physically sensible 2D extension of the 1D concept of throat area, as opposed to placing a ruler across the narrowest point of passage to obtain a geometric throat area.

For a fully choked streamline, flow conditions upstream of the sonic line are independent of those downstream. This facilitates an analytical approach where the flow conditions immediately upstream of any choked streamline's sonic point are treated as a known state. That streamline's mass flow rate is wholly a function of that state, thus the mass flow rate of a fully choked 2D nozzle is wholly a function of its A_{eff} as derived from its sonic line. For an unchoked streamline, its mass flow rate is a function of the state of every point along the streamline, including points downstream of where sonic conditions would appear in choked cases. It is thus advantageous to supplement design-condition simulations with simulations at a pressure ratio where the nozzle guide vane is guaranteed fully choked, allowing for analysis of a fully-formed sonic line and computation of a corresponding A_{eff} .

The present study will nonetheless discuss the reasons for which geometric throat area remains a useful predictor of NGV flow capacity in many cases, as has been noted in the literature. Deepak Thirumurthy et al [2] discussed the challenges and uncertainties associated with the accurate matching of an aeroderivative gas generation turbine. The authors' focus was on various means of predicting capacity to facilitate proper matching. The authors noted that "the throat area of any blade or vane row has a strong influence on the overall capacity of the turbine. The vane or blade throat plane...is defined as the plane formed by the smallest passage area normal to the flow path. The effects are of first order when the throat area is changed for the first stage of the turbine." The prior discussion of effective area is in agreement with this statement. If 2D nozzle throat width is varied in a way that does not significantly affect the sonic line shape, effective area and thus choked mass flow rate would be expected to vary to first order. This hypothesis will be tested in this chapter.

2.1 Nozzle guide vane capacity uncertainty in 2 dimensions

The immediate challenge in quantifying 2D nozzle flow capacity is that analytical approaches are incomplete. If any nozzle's A_{eff} could be inferred from its geometry, it would be possible to investigate the effects of the geometry on the flow capacity to a high degree of accuracy, but the only way to find A_{eff} is to solve the flow computationally to obtain the $M = 1$ line. Once a CFD solution has been obtained, the flow capacity is necessarily also obtained. Those concerned with mapping NGV geometry onto flow capacity are thus presented with 2 options: either perform CFD on every conceivable shape of NGV and create a lookup table of arbitrary fidelity, or analyse a relatively small set of CFD solutions to create heuristics about what types of geometric changes cause what types of changes to the shape of the $M = 1$ line and local flow vectors.

2.1.1 Geometry, mesh, and boundary conditions

Rolls-Royce plc have provided the present study with a family of NGV geometries suitable for such an approach, all from the Trent 900 engine. Geometric variation among Trent 900 NGVs has been subject to extensive measurement by Rolls-Royce. In one such set of studies, Terry Hall [3] and Giulio Zamboni [4] provided geometric definitions of 6 NGVs. These studies considered 2 slightly different production standards within the Trent 900 NGV family, which are referred to by the company as the M-skew standard and the EP1 standard. Rolls-Royce randomly selected three production NGVs from each standard and measured their surface geometries using the *white light/GOM* scanning method. This resulted in the geometric definition files which were provided to the present study by Hall and Zamboni. These files do not include film cooling holes or the trailing edge slot. The trailing edges are smoothly rounded.

Significant variations exist among the geometry of the 6 NGVs, even when cooling features are not accounted for. Zamboni described the process for quantifying these variations in 3D, which will be discussed in Section 2.2. The present study defined an approach for deriving 2D geometries from the 3D files and quantifying the variations among them.

The 3D NGV surface shape was provided by Rolls-Royce as a set of co-ordinates which define 21 closed loops on the vane surface. Each loop consists of a pair of streamlines which diverge from a stagnation point on the vane's leading edge and converge at the trailing edge. The 11th loop was thus considered to be the closest approximation to a mid-span slice of the NGV. MATLAB was used to process the 3D curve of the 11th loop, producing a 2D section via the following process.

1. Project the loop's coordinates onto a cylindrical surface whose radius is equal to the NGV annular radius at mid-span.
2. Periodically repeat the resulting shape in the circumferential direction to create an annulus of 2D vanes wrapped around the cylinder.
3. Transform the annulus into an infinite 2D linear cascade by taking the circumferential coordinate to be a vertical coordinate.

This process is illustrated in Figure 2.2.

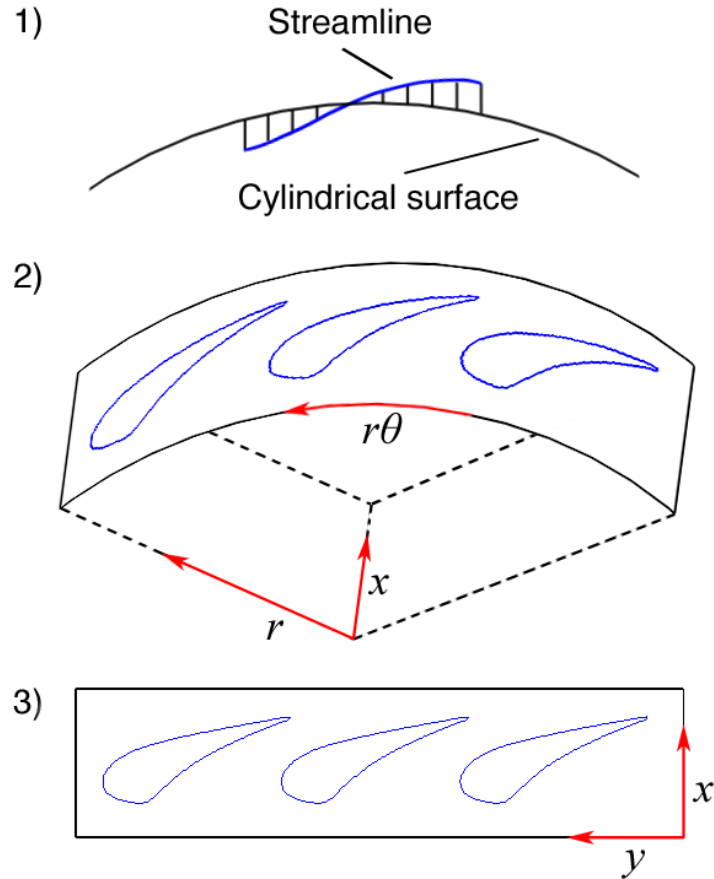


Figure 2.2: Creation of 2D mid-span approximation of NGV geometry

The resulting coordinates were connected to form a closed body. This body was placed in a computational domain consisting of a straight inlet section, a curved turning section, and a straight outlet section inclined at the NGV turning angle. The domain was modelled in Ansys Fluent, where the inlet boundary was specified to have total pressure p_{01} and the outlet boundary was specified to have static pressure p_2 . The remaining domain boundaries were made periodic with one another to preserve the 2D linear cascade. The NGV surface boundary was specified as a solid wall with a no-slip boundary condition and no heat conduction. The resulting computational domain is illustrated in Figure 2.3. On the outlet boundary, labels 0 and 1 denote the start and end points for the wake surveys that will be presented in Chapter 3.

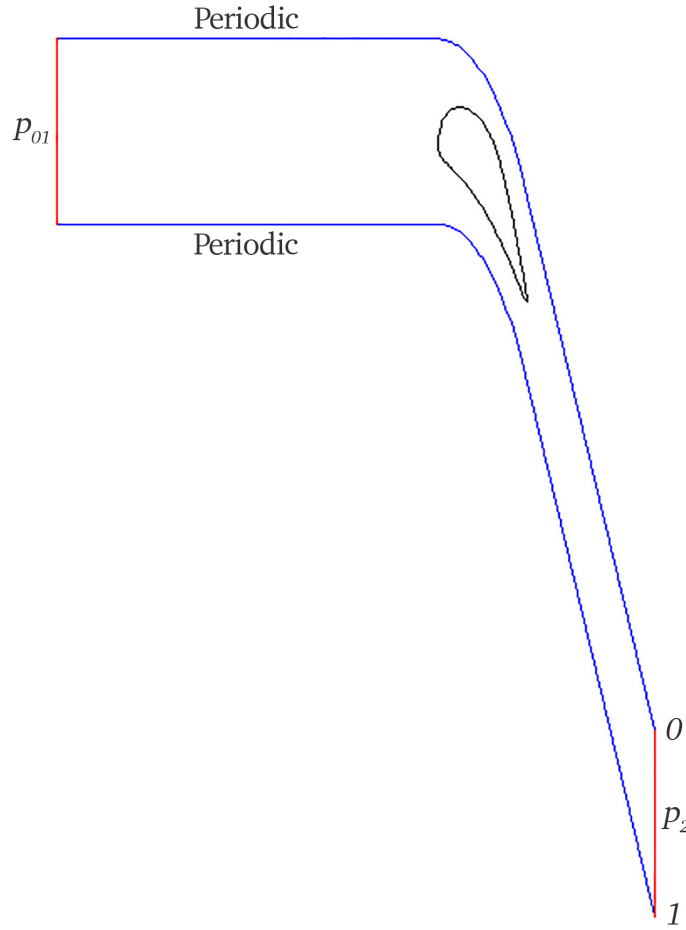


Figure 2.3: Computational domain and boundaries

This configuration has been the basis for all other 2D CFD analyses in the present study, where additional boundaries are added to account for cooling features as required. Values for the simulation were set according to Table 2.1.

Table 2.1: Boundary conditions at design pressure ratio for multi-vane capacity study

Parameter	Value
NGV series	Rolls-Royce Trent 900
NGV turning (degrees)	76.89
Inverse pressure ratio $\frac{P_{01}}{P_2}$	1.79, 3.33
Inlet total pressure (Pa)	4.33×10^6
Inlet total temperature (K)	300
Outlet static pressure (design) (Pa)	2.42×10^6
Outlet static temperature (Pa)	300
Solver type	Density-based
Cell count	35,000

For turbomachinery flows of this type, the boundary layer thickness will be shown to be large enough to significantly affect the NGV throat area. The mesh must resolve the whole boundary layer within a

region of high resolution which is sufficiently large to cover the maximum boundary layer thickness. The maximum thickness of a turbulent boundary layer is approximated by the formula

$$\delta \approx 0.37 \frac{L}{Re^{\frac{1}{5}}} \quad (2.2)$$

where L is the characteristic length in the direction of the flow (the approximate NGV chord length) and Re is the Reynolds number. The Reynolds number is defined as

$$Re = \frac{uL\rho}{\mu} \quad (2.3)$$

where u is a representative value for flow velocity and μ is the dynamic viscosity of the fluid within the temperature range of the flow. For compressible flow, the velocity and density are substituted to give

$$Re = \frac{M \sqrt{\gamma RT} L \frac{p}{RT}}{\mu} \quad (2.4)$$

which simplifies to

$$Re = \frac{L}{\mu} \sqrt{\frac{\gamma}{R}} \frac{p}{\sqrt{T}} M \quad (2.5)$$

$$Re = \frac{L}{\mu} \sqrt{\frac{\gamma}{R}} \frac{p_0}{\sqrt{T_0}} M \frac{\left(1 + \frac{\gamma-1}{2} M^2\right)^{-\frac{\gamma}{\gamma-1}}}{\sqrt{\left(1 + \frac{\gamma-1}{2} M^2\right)^{-1}}} \quad (2.6)$$

$$Re = \frac{L}{\mu} \sqrt{\frac{\gamma}{R}} \frac{p_0}{\sqrt{T_0}} M \left(1 + \frac{\gamma-1}{2} M^2\right)^{\frac{\gamma+1}{2(\gamma-1)}} \quad (2.7)$$

Equation 2.7 was used to compute a Reynolds number for the case of choked or near-choked NGV flow with the following values, based on the values specified in Table 2.1.

Table 2.2: Values for calculating NGV Reynolds number

Parameter	Value
L	0.08 m
μ	19×10^{-6} Pas
p_0	4.33×10^6 Pa
T_0	300 K
γ	1.4
R	$287 \text{ Jkg}^{-1}\text{K}^{-1}$
M	1

This resulted in a value of $Re = 4.2 \times 10^7$. Maximum boundary layer thickness was thus estimated using equation 2.2 to be 1 mm. This is of the order of 10% of the NGV throat width, so full resolution of the boundary layer is required for any CFD study of the effects of NGV geometric changes.

The NGV surface was enclosed in a structured quadrilateral mesh which extended out by 2 mm. Compared to the estimated maximum boundary layer thickness, the factor of 2 ensured that the whole boundary layer was captured, reduced the gradient of cell size change within the boundary layer mesh, and provided additional resolution within the base region downstream of the trailing edge, where boundary layer separation and entropy generation occur amid high surface curvature.

Full resolution of the boundary layer required placement of mesh elements within the laminar sub-layer. Regions within the boundary layer were assumed to be divided according to the *universal law of the wall*. This boundary layer model is derived from experimental measurements and dimensional analysis performed by Johann Nikuradse [5]. The author's motivation was the need to predict the velocity profile and thickness of turbulent boundary layers, given the free-stream conditions. The work is of renewed importance in the context of contemporary CFD such as the present study, where knowledge of appropriate boundary layer mesh resolution is mandatory.

Nikuradse showed that turbulent boundary layers in general exhibit a high degree of dimensional similarity if distance from the wall y is appropriately non-dimensionalised. The assumption was that qualitatively distinct regions of the boundary layer may be characterised by a dimensionless number that takes the place of y . Regions closer to the wall are expected to be dominated by viscous forces, and regions closer to the free-stream are expected to be dominated by inertial forces. The dimensionless wall distance parameter is thus expected to take similar form to the Reynolds number. It is defined as

$$y_+ = \frac{u_f y \rho}{\mu} \quad (2.8)$$

where u_f is the friction velocity, defined as

$$u_f = \sqrt{\frac{\tau_w}{\rho}} \quad (2.9)$$

where τ_w is the shear stress at the wall boundary. Equation 2.9 thus characterises the wall shear stress as a velocity which is used in the Reynolds-type formulation of Equation 2.8. τ_w is defined as

$$\tau_w = \frac{1}{2} C_f \rho u^2 \quad (2.10)$$

where C_f is a coefficient of skin friction and u is the free-stream velocity. C_f may be computed from the free-stream Reynolds number according to the correlation proposed by Hermann Schlichting [6]

$$C_f = (2 \log_{10} Re - 0.65)^{-2.3} \quad (2.11)$$

For compressible flows, equation 2.10 may be expressed as

$$\tau_w = \frac{1}{2} C_f \frac{p}{RT} M^2 \gamma RT \quad (2.12)$$

$$\tau_w = \frac{1}{2} C_f \gamma p_0 M^2 \left(1 + \frac{\gamma-1}{2} M^2\right)^{-\frac{\gamma}{\gamma-1}} \quad (2.13)$$

allowing a compressible expression of u_f as

$$u_f = \sqrt{\frac{\frac{1}{2} C_f \gamma p_0 M^2 \left(1 + \frac{\gamma-1}{2} M^2\right)^{-\frac{\gamma}{\gamma-1}}}{\rho_0 \left(1 + \frac{\gamma-1}{2} M^2\right)^{-\frac{1}{\gamma-1}}}} \quad (2.14)$$

$$u_f = \sqrt{\frac{C_f \gamma R T_0 M^2}{2 + (\gamma - 1) M^2}} \quad (2.15)$$

and allowing a compressible expression of y_+ as

$$y_+ = \sqrt{\frac{C_f \gamma R T_0 M^2}{2 + (\gamma - 1) M^2} \frac{y}{\mu} \frac{p_0}{R T_0} \left(1 + \frac{\gamma-1}{2} M^2\right)^{-\frac{\gamma}{\gamma-1}}} \quad (2.16)$$

$$y_+ = \frac{y}{\mu} \sqrt{\frac{\gamma}{R}} \frac{p_0}{\sqrt{T_0}} \sqrt{\frac{C_f}{2}} M \left(1 + \frac{\gamma-1}{2} M^2 \right)^{\frac{\gamma+1}{2(1-\gamma)}} \quad (2.17)$$

This expression is of similar form to the expression for Reynolds number in equation 2.7. Both are shown to be a function of Mach number and of the upstream conditions $\frac{p_0}{\sqrt{T_0}}$. If these expressions are normalised against the upstream conditions in a similar way to flow capacity, it is shown that both the dimensionless speed Re and the dimensionless boundary layer thickness y_+ are purely functions of Mach number and of a geometric parameter – L and y respectively. This is subject to the assumptions that μ is approximately constant within the range of temperatures and $\sqrt{\frac{C_f}{2}}$ is approximately constant for sufficiently high Reynolds numbers.

Equation 2.17 may be rearranged to compute a real distance y from the wall given a value of y_+ . In the general case of turbulent boundary layers, the laminar sublayer occupies the region of $y_+ < 5$. The present study placed the first layer of mesh nodes at a wall distance of $0.3 \mu\text{m}$ corresponding to a y_+ value of 5. This is in accordance with a study of laminar sublayer resolution by Salim M. Salim and Siew-Cheong Cheah [7].

Within the structured boundary mesh, element size was grown so that the outermost elements had an aspect ratio of approximately $\frac{1}{2}$. Beyond this, the domain was populated with an unstructured quadrilateral-dominant mesh. Node distributions along the two periodic boundaries were made identical, and nodes adjacent to the structured boundary layer mesh were made to match its outermost node distributions. Within the general domain, unstructured mesh generation was automated using Ansys Fluent's built-in meshing feature. The resulting mesh formed the basis for all other 2-dimensional NGV meshes in the study. The mesh and periodic pattern are depicted in Figure 2.4 and details of the mesh, showing the structured boundary layer treatment, are depicted in Figure 2.5.

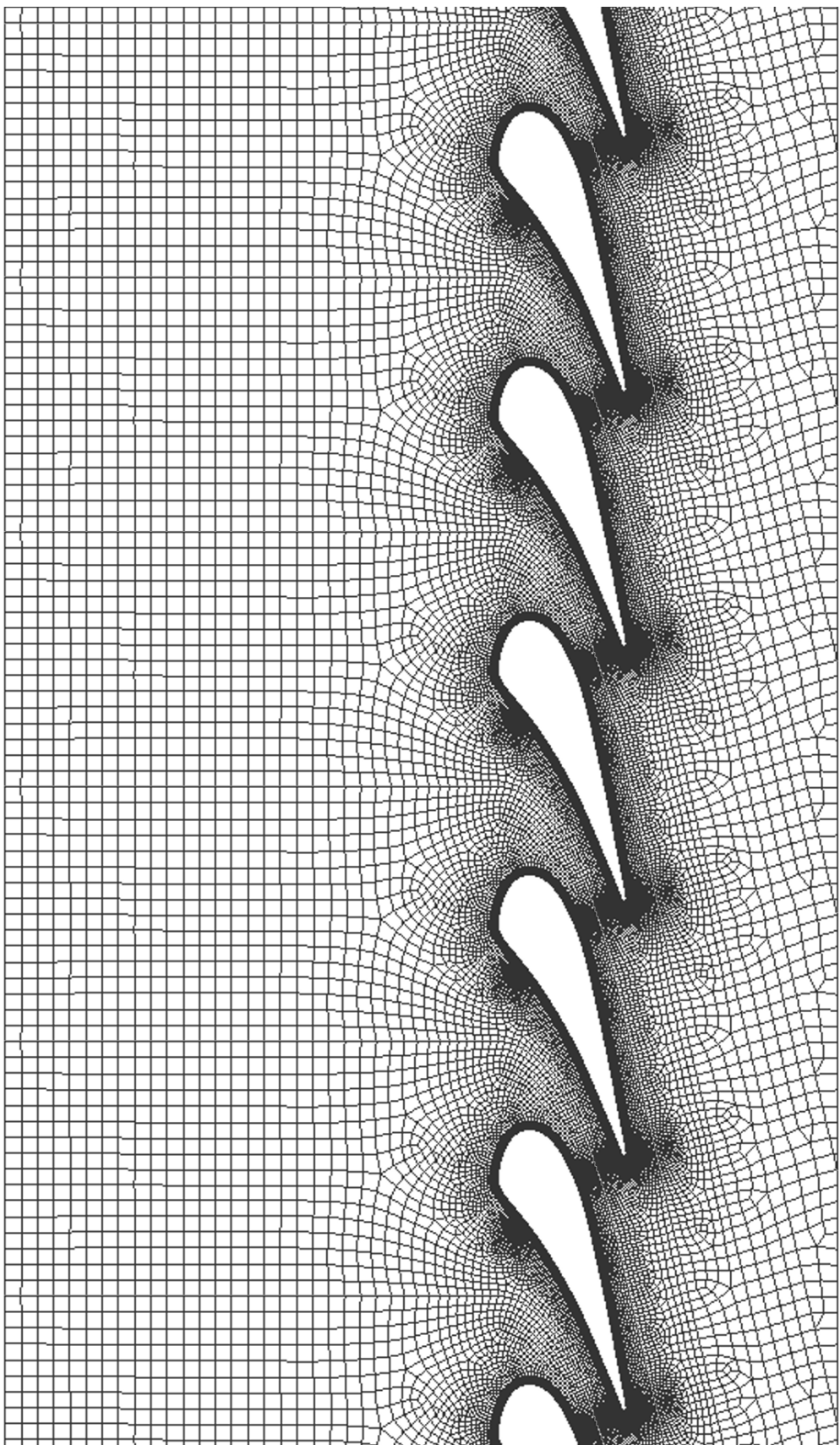


Figure 2.4: Mesh for Trent 900 throat width variation study

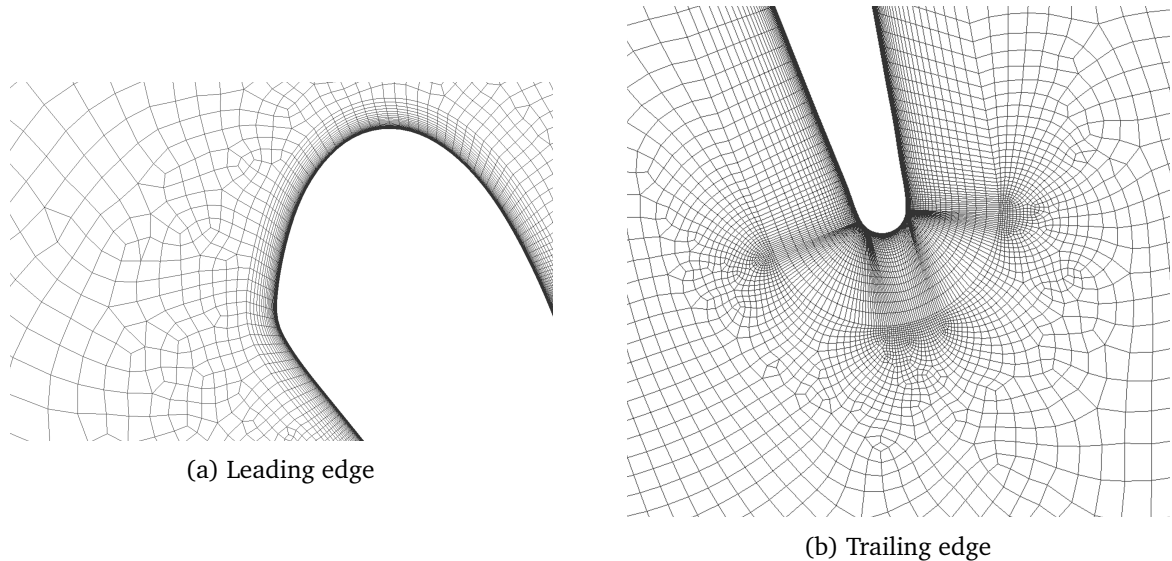


Figure 2.5: Details of mesh for Trent 900 throat width variation study

The described mesh and boundary condition specifications were used to perform a series of CFD simulations of each of the 6 2D NGVs in Ansys Fluent. Solutions were initialised using the solver's built-in FMG initialisation. This procedure automatically constructs a coarser version of the supplied mesh, on which an initial solution is converged before refinement to the final resolution. More detailed explanation of the scheme is provided by Ansys [8]. A script in the Fluent Journal language was used to produce solutions at incrementally increasing inverse pressure ratios of between 1.5 and a fully choked inverse pressure ratio of 3.33. NGV mass flow rate was saved at each pressure ratio. Full solution data were saved for the final fully choked pressure ratio to enable analysis of the shocks, expansions and sonic line at choked conditions. There were 32 increments and typical overall solution times were approximately 10 hours. The SST-k ω turbulence model was used.

2.1.2 Effect on 2D capacity

Figure 2.6 shows contours of Mach number for one of the 6 solutions at a fully choked pressure ratio. Figure 2.7 shown contours of Mach number for the same solution in the throat region.

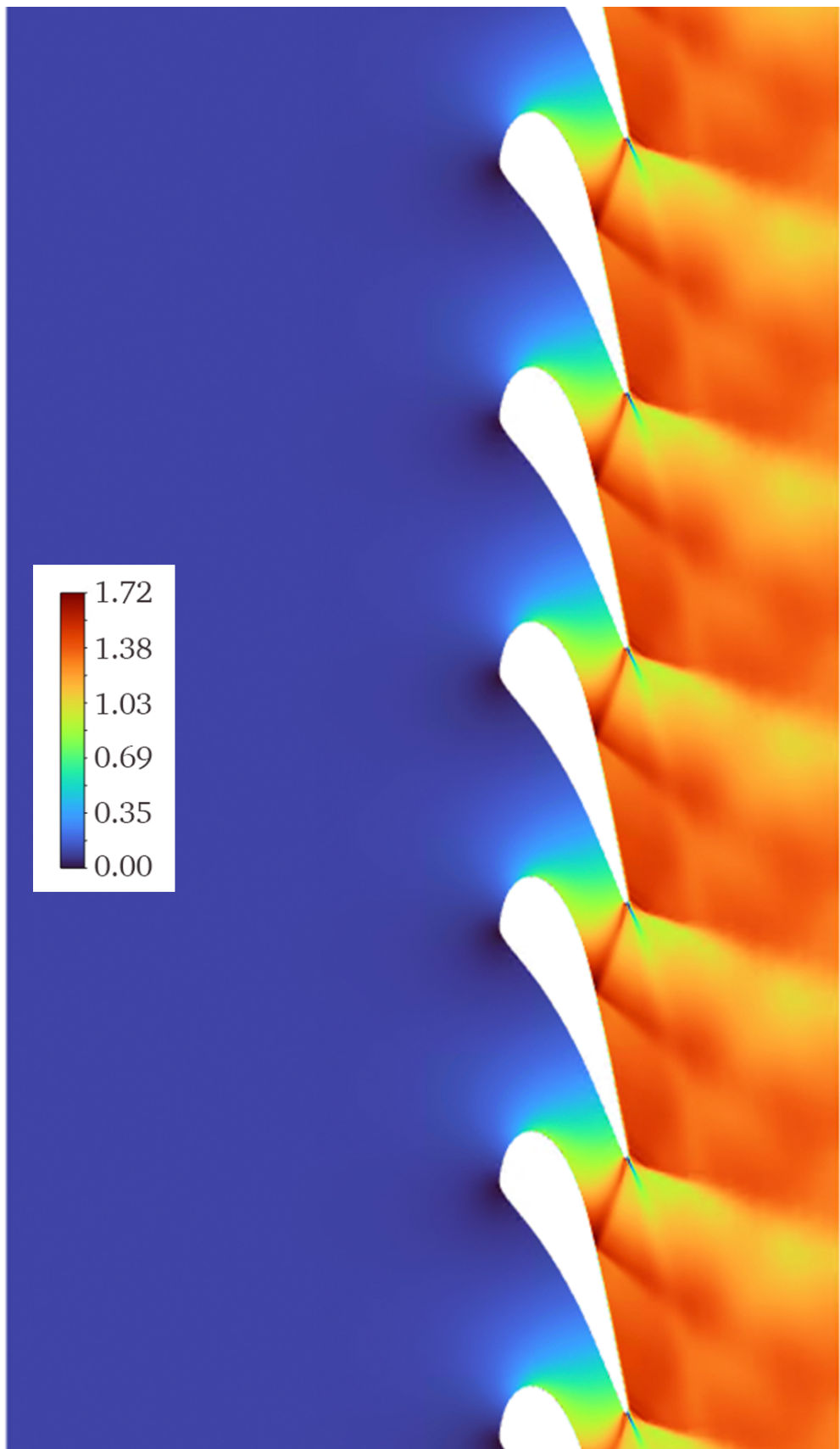


Figure 2.6: Contours of Mach number for whole solution on vane KSZ03 at $\frac{p_{01}}{p_2} = 3.33$

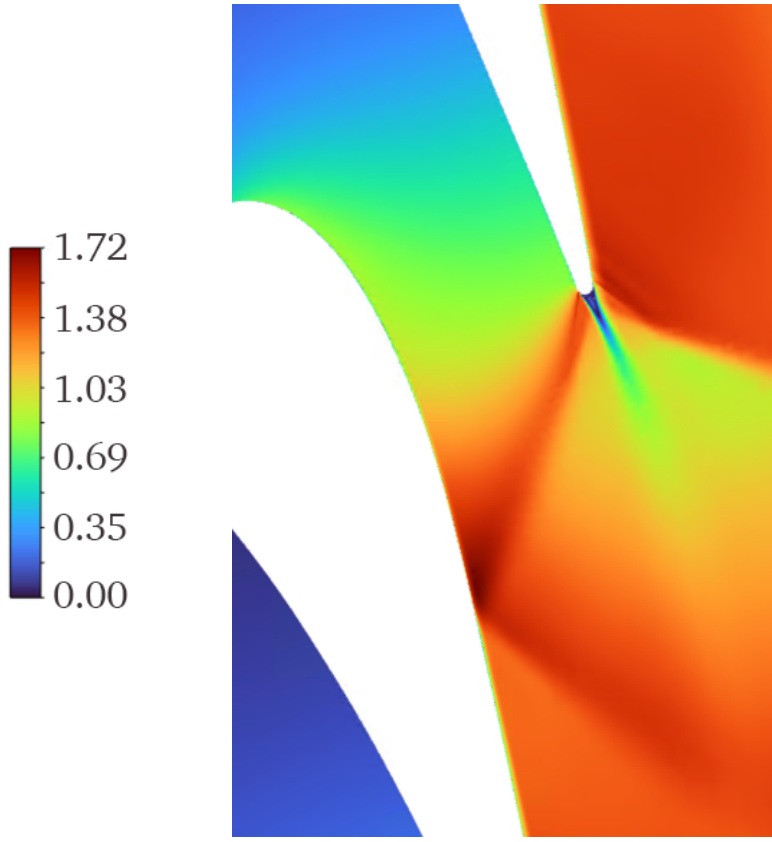


Figure 2.7: Contours of Mach number for solution near throat on vane KSZ03 at $\frac{p_{01}}{p_2} = 3.33$

Figures 2.6 and 2.7 illustrate the presence of developed supersonic flow phenomena downstream of the throat. These include expansion fans as the flow traverses the convex region around the NGV trailing edge (which is not shaped this way in reality) and shockwaves induced as the flow traverses the concave region produced by the trailing edge wake. The pressure side shockwave reflects off the suction side of the adjacent NGV in a similar fashion to supersonic nozzle shock diamonds. These phenomena are in agreement with commonly seen flow features of NGVs in the supersonic regime. Figure 2.7 also illustrates the growth of a boundary layer on the suction side of the NGV. This boundary layer's interaction with the sonic line will be subsequently discussed in the context of its effect on flow capacity.

Figure 2.8 plots percentage changes in the flow capacity of the 6 NGVs (defined by equation 1.13 and quantified by the upstream boundary conditions in Table 2.1) against inverse pressure ratio $\frac{p_{01}}{p_2}$.

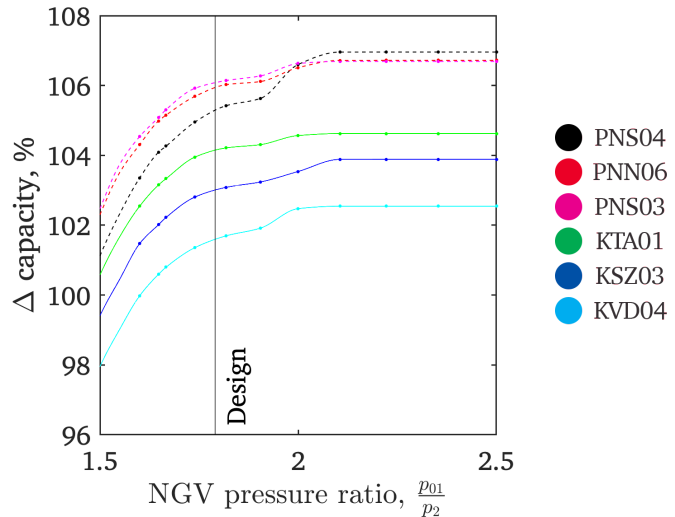


Figure 2.8: 2D capacity trends for 6 Trent 900 NGVs

Differences are seen to exist between the capacity trends of the 6 NGVs. Across the range of pressure ratios, all 6 NGVs exhibited a range of approximately 4% capacity difference. Although the NGVs were all fully choked at the greatest inverse pressure ratio, separate NGVs became choked at significantly different pressure ratios, suggesting that the formation of transonic flow features occurred in different locations between the 6 NGVs. The capacity trends are seen to be broadly divided between the M-skew family (K- serial numbers) and the EP1 family (P- serial numbers). The 3 M-skew NGVs had comparatively lower flow capacities than the EP1 NGVs at all pressure ratios. The capacities of the EP1 NGVs had comparatively small variation from one another across pressure ratios, but their homogeneity was broken by vane PNS04, which had the lowest flow capacity of the family at low inverse pressure ratio, but switched to have the highest flow capacity at high inverse pressure ratio.

The differing capacity trends may be further discussed by inspecting the shape of the $M = 1$ lines formed in the throat regions of the 6 NGVs at a fully choked pressure ratio. These $M = 1$ lines are depicted in Figure 2.9 along with the lines of minimum length between the adjacent NGVs of each standard.

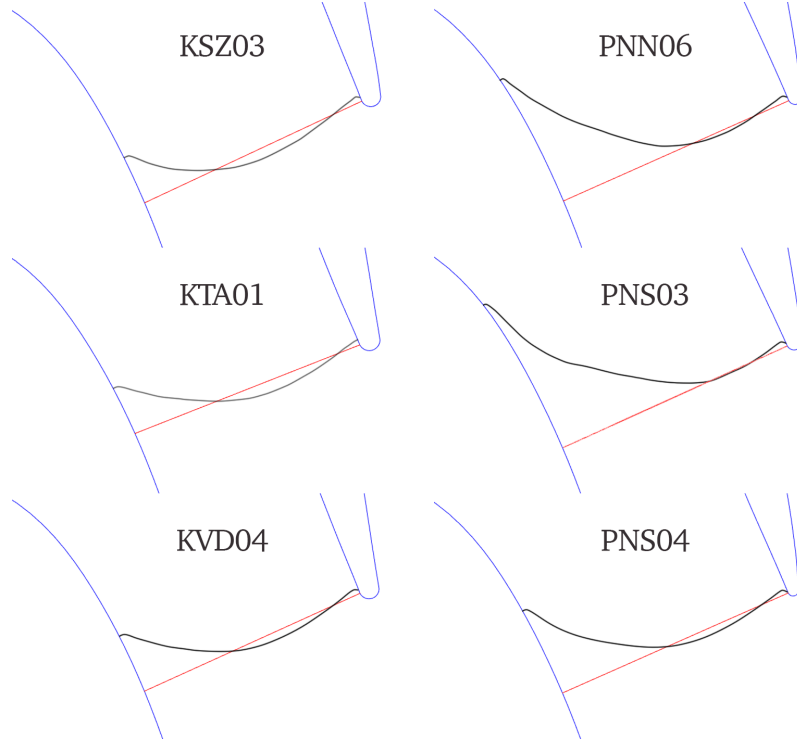


Figure 2.9: Sonic lines for 6 Trent 900 NGVs at $\frac{p_{01}}{p_2} = 3.33$

In Figure 2.9, a trend is visible of the M-skew sonic lines exhibiting smaller deviation from the line of minimum width, compared to the sonic lines of the EP1 NGVs. This suggests that a design choice resulted in a difference in the aerodynamics of the two families of NGV, such that upstream regions of the EP1 flow field reached sonic conditions significantly further upstream of the geometric throat compared to the M-skew flow field. Vane PNS04 presented a significantly different sonic line shape which is taken to correspond to its significantly different capacity trend compared to the other 2 vanes in its family. It is suggested that its relatively flow-orthogonal sonic line is caused by aerodynamic features that also cause its relatively sudden increase in capacity prior to choking. This cannot be confirmed in the absence of a statistically significant number of NGV geometries to compare.

Matlab was used to calculate the minimum throat width of each 2D NGV. The resulting values are given in Table 2.3.

Table 2.3: Throat widths of 6 Trent 900 NGVs

Production standard	Serial number	Throat width (mm)
M EP1	PNS04	12.7
	PNN06	12.7
	PNS03	12.7
M-skewed	KTA01	12.5
	KSZ03	12.4
	KVD04	12.2

Discussion is warranted of the relationship between flow capacity and throat area. Consideration is to be made of both throat area in its pure geometric form A , and its effective from A_{eff} as defined in

equation 2.1. Figure 2.10 plots the 6 NGVs' variations in capacity at design pressure ratio against their variations in geometric throat width. Both axes are normalised against the largest values in the set. The averages of the M-skew and EP1 families are plotted and lines of gradient 1 are plotted intersecting the average values, such that any deviations from 1-dimensional compressible flow correspond to deviations from the lines of gradient 1.

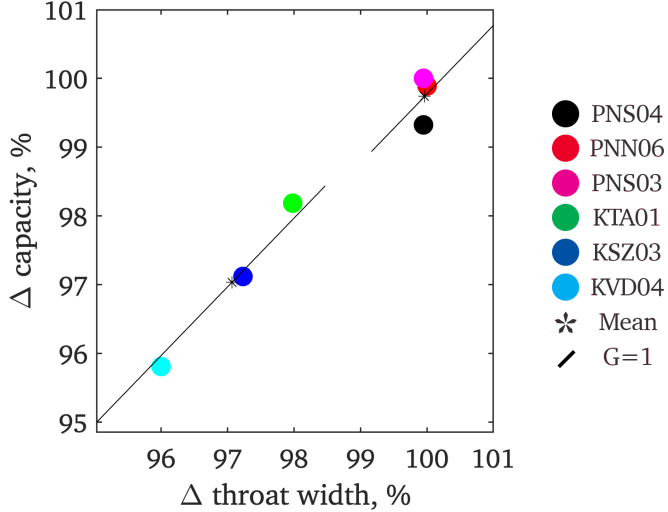


Figure 2.10: 2D NGV capacity percentage delta as a function of 2D throat width for 6 NGVs at $\frac{p_{01}}{p_2} = 1.79$ (design)

The 6 NGVs are seen to approximately conform to a directly proportional relationship between geometric throat width and flow capacity, suggesting that geometric throat width is a good estimator of flow capacity among NGVs without significant differences in aerodynamic design. The M-skew vanes exhibited notable conformity to this trend. This is in agreement with the observed homogeneity between the M-skew sonic line shapes. It is suggested that, among the 3 vanes, the 2-dimensional sonic line shapes were scaling linearly with the shape of the geometric throat line, resulting in the observed linear relationship between geometric throat width and flow capacity despite the presence of a 2D flow field. 2D flow features appear to scale proportionately provided the sonic line scales proportionately. In contrast, no correlation was observed between throat area and flow capacity among the EP1 NGVs. Speculation may be limited to the observation that the qualitatively distinct PNS04 vane exhibited significantly lower flow capacity than the other 2 despite having almost identical geometric throat areas.

Although NGV throat width is a good predictor of NGV flow capacity if aerodynamics do not vary significantly, it is not useful if the sonic line is subject to unpredictable changes in shape and location. The resulting heuristic fails to account for the fact that the majority of streamlines within the flow reach sonic conditions at a point other than their point of minimum width. This discrepancy may be investigated by quantifying the effective throat width of each case, instead of the geometric throat area. Matlab was used to implement the integral

$$A_{eff} = \int_1^2 \hat{\mathbf{v}} \cdot \hat{\mathbf{r}} dL \quad (2.1)$$

To achieve this, results for M and x and y velocity components were exported from each Fluent solution. These data were imported into Matlab and interpolated onto a structured quadrilateral grid which covered the region around the throat between 2 adjacent NGVs. Within this domain, data points corresponding to the $M = 1$ line were identified using an algorithm to detect the cross-over

from $M < 1$ to $M > 1$. A subsequent algorithm was used to order and connect these points into a sonic line. It was then possible to compute the local velocity unit vector \hat{v} and local unit vector orthogonal to the sonic line \hat{r} at each point, and to perform the integral. This resulted in Figure 2.11, which plots the 6 NGVs' variations in capacity at design pressure ratio against their variations in effective throat width. Both axes are normalised against the largest values in the set. Because the concept of A_{eff} is designed to account for generalised variations between NGVs, Figure 2.11 does not group the NGVs into 2 separate families.

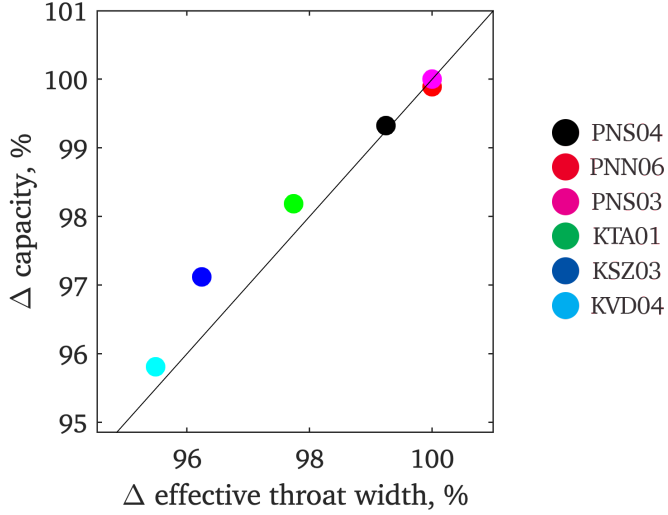


Figure 2.11: 2D NGV capacity percentage delta as a function of 2D A_{eff} for 6 NGVs at $\frac{p_{01}}{p_2} = 1.79$ (design)

Figure 2.11 demonstrates the viability of the A_{eff} approach. All six vanes approximately show a directly proportional relationship between flow capacity and effective throat width. This is in agreement with the assumption that the integral definition of A_{eff} amounts to the summation of the 1-dimensional throat widths of every streamline in the flow. However, 3 of the NGVs exhibit significant deviation from direct proportionality, suggesting that the use of the sonic line fails to account for regions of the flow which remain subsonic given that the flow is largely unchoked. A possible refinement to the A_{eff} approach may be to combine it with a prediction of the boundary layer thicknesses at the points where the sonic line meets the suction side and pressure side of the NGVs. Heuristics may be developed to relate the touch-down points with the predicted boundary layer thicknesses and thus the degree of A_{eff} over-estimation caused by the inclusion of subsonic flow. This would result in a metric which is directly proportional to choked 2D capacity and closely correlated with 2D capacity at the design pressure ratio.

A_{eff} remains computable only in the event that a CFD solution has been obtained, by which point flow capacity is already predicted. The next goal is to find an aspect of NGV geometry which can be shown to have a reliable effect on the shape of the $M = 1$ line. In this way, the geometric change will have been shown to account for a known change in A_{eff} , which has itself been shown to account for known changes in flow capacity in 2 dimensions. Since the M-skew and EP1 families exhibit clear differences in the degree of pre-throat sonic conditions which are present, future studies may examine whether NGVs can be reliably designed to have sonic lines whose shape is predictable. If the sonic line is known by design to be approximately orthogonal to the flow and non-susceptible to fluctuation, it is safe to rely on just 2D geometric throat width to predict variations in NGV flow capacity in 2 dimensions.

2.2 Comparison of 2D capacity predictions with 3D data

The present study compared the 2D data presented in Section 2.1 with Rolls-Royce's 3D CFD predictions of the flow capacities of the same 6 NGVs. The motivation was to analyse the differences between the 2D throat length vs capacity relationship and the 3D throat area vs capacity relationship. The analytical techniques of Section 2.1 were translated to this 3D relationship where possible.

2.2.1 Effect on 2D capacity versus 3D capacity

Figure 2.12 plots percentage changes in the flow capacity of the 6 NGVs (defined by equation 1.13 and quantified by the upstream boundary conditions in Table 2.1) against inverse pressure ratio $\frac{p_{01}}{p_2}$.

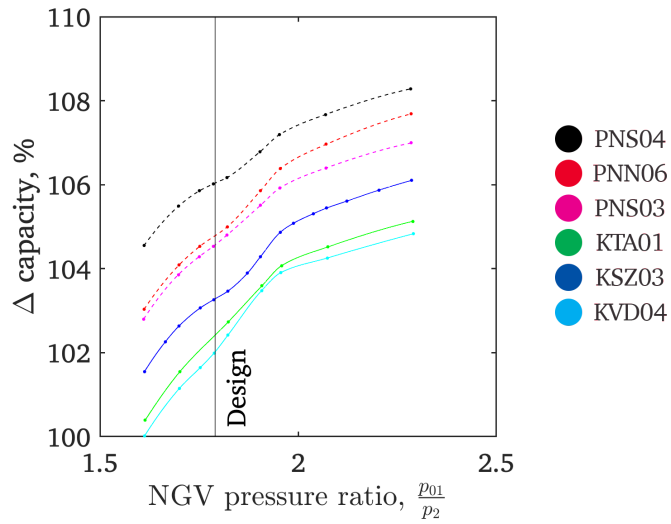


Figure 2.12: 3D capacity trends for 6 Trent 900 NGVs

The predominant feature of Figure 2.12 is that none of the NGVs reaches a choked condition at pressure ratios that resulted in a fully choked condition in the 2D simulations. This suggests that there are significant incursions into the flow from subsonic secondary flows. This alone is sufficient to preclude the present A_{eff} approach in these 3D cases, since it has been shown to be limited even by the presence of thin boundary layers in the 2D cases. In this case, an $M = 1$ surface may not exist in a useful sense.

Zamboni defined the Rolls-Royce process for calculating 3D throat area as follows: "Along each vane span section, the throat line is defined as that line which connects the TE of one vane with the point of minimum distance on the suction surface of the nearby vane in the tangential direction. For a vane with TE slot, the TE point is defined as the start of the cut back... The throat surface interpolates all the throat lines spanwise." Their study produced values for throat area of the 6 NGVs in question. These values are listed in Table 2.4.

Table 2.4: Throat areas of 6 Trent 900 NGVs

Production standard	Serial number	Throat area (mm ²)
M EP1	PNS04	1598.8
	PNN06	1592.0
	PNS03	1587.2
M-skewed	KTA01	1584.6
	KSZ03	1578.4
	KVD04	1571.4

The viability of the geometric throat area approach to 3D data is illustrated in Figure 2.13, which plots the 6 NGVs' variations in capacity at design pressure ratio against their variations in geometric throat area. Both axes are normalised against the largest values in the set. The averages of the M-skew and EP1 families are plotted and lines of gradient 1 are plotted intersecting the average values, such that any deviations from 1-dimensional compressible flow correspond to deviations from the lines of gradient 1.

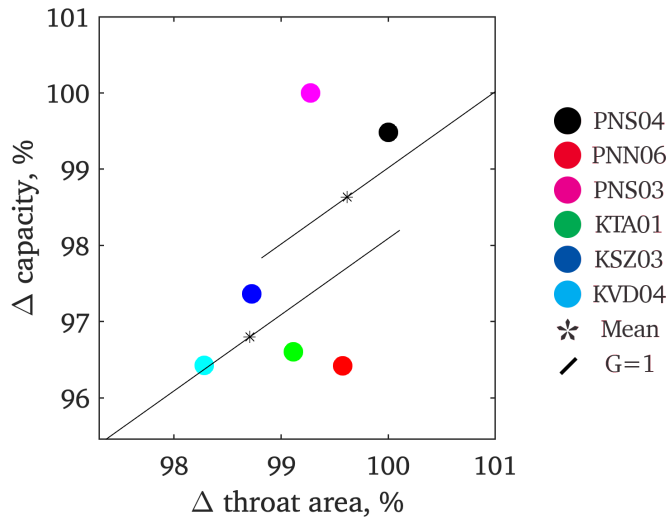


Figure 2.13: 3D NGV capacity percentage delta as a function of 3D throat area for 6 NGVs at $\frac{p_{01}}{p_2} = 1.79$ (design)

Figure 2.13 shows that no correlation exists between geometric throat area and flow capacity for the 6 NGVs simulated by Rolls-Royce. This is in agreement with the hypothesis that highly 3-dimensional flow phenomena are present to a degree that predominates over any area-capacity relationship. Future study might divide focus between developing a 3D version of the A_{eff} technique and accessorising it with a model for the subsonic secondary flows that are hypothesised to be present even at the fully choked pressure ratio used to evaluate A_{eff} in the 2D cases. An overarching goal may be to confirm that secondary flows are indeed the confounding factor that is not captured by 2-dimensional CFD. In any case, motivation is presented to resolve the failure of present analytical techniques in understanding the sensitivity of nozzle guide vane flow capacity to geometric changes.

2.3 Chapter conclusions

Variations in the cast shape of nozzle guide vanes have been shown to cause variations in their predicted flow capacity. 2D CFD simulations have been performed on a family of 6 NGVs which were selected by Rolls-Royce to be representative of random variations in the shape of Trent 900 engine parts after they have been cast but before cooling features have been machined in.

At the NGVs' design inverse pressure ratio, the design flow capacity of the 6 vanes has been found to correlate to some extent with both the vanes' geometric throat area and with the effective throat width A_{eff} . 2D geometric throat width can be evaluated from the NGV design geometry without any further computational effort, but A_{eff} cannot be evaluated without obtaining a CFD solution at a fully choked pressure ratio. The A_{eff} approach is thus offered not as a means to predict the flow capacity of a given geometry, but rather as a means to quantify the shape of the 2-dimensional sonic line that forms at a fully choked pressure ratio, and to discuss this shape's effect on capacity.

Nozzle guide vane flow capacity correlates well with A_{eff} at the design pressure ratio despite the non-existence of a sonic line when the flow is not fully choked. This suggests that the sonic line shape is driven by the same geometric factors that drive the 2-dimensional flow field prior to choking. Thus for a given NGV production standard that outputs sets of vanes with casting variations, two conclusions can be drawn from simulating a representative sample of the vanes in 2D. Firstly any scanned vane's 2D capacity will be well-predicted by its 2D throat width if fully choked simulations have shown the sonic line to exhibit relatively small deviation from the geometric throat line. Secondly the whole production standard is likely to have reduced capacity predictability if fully choked simulations have shown the sonic line to vary significantly in shape between individual vanes.

Conclusions are more difficult to draw in the case of 3D capacity, where a 3D extension of the A_{eff} approach is rational but would require careful adjustment for the delayed onset of choking in 3D compared to 2D. Where Section 2.1 suggested a boundary-layer model as a future addition to the technique, Section 2.2 has presented data from 3D geometries for which the equivalent inverse pressure ratio of 3.33 would produce significant regions of secondary flow which are not choked. These regions may be accounted for by an appropriate model or negated by the use of an even higher inverse pressure ratio. The overall conclusion of this chapter is that future analyses of casting variations versus flow capacity should involve 3D simulation, should account for both boundary layers and secondary flows when conceptualising A_{eff} in 3D, and should use a statistically significant number of scanned vanes to produce two key metrics. Firstly the mean departure of the vanes' sonic surfaces from the surface of minimum area will reveal whether the minimum area is a useful capacity predictor for that production standard. Secondly the variance of the vanes' sonic line shapes will indicate that production standard's capacity uncertainty.

Chapter 3

Trailing edge

Nozzle guide vane flow capacity is known to be a function of effective throat area. Thus we must survey the practical reasons for which effective throat area might vary. In a real engine, NGV effective throat area may depart from its design value if the NGVs depart from the ideal aerodynamic design shape. This may occur through practical design choices for reasons such as cooling or blockage avoidance, because of the finite precision of manufacturing, or because of erosion while in service.

A goal of the present study is to help ascertain how much such design decisions and off-design conditions affect the predictability of NGV flow capacity, and to comment on ways to mitigate this limitation. The NGV trailing edge is an area of focus because it is particularly susceptible to both finite-precision and in-service departures from its design shape.

The trailing edge is susceptible to finite-precision departures from its design shape because of how it is manufactured. Vane pairs are cast to a finite precision as discussed in Section 2.1, where significant geometric variation appears even prior to the addition of cooling features. The vanes are then machined to finish off the trailing edge shape to a high tolerance. The finishing creates the aerodynamically best possible trailing edge.

The trailing edge's principal design feature is the difference between the amount of material left on the suction side of the coolant ejection slot and the amount left on the pressure side. This creates the thinnest possible final trailing edge for the vane with the intent of minimising separated wake area and thus loss. The resulting feature will be referred to as the end-edge in this thesis, and is illustrated in Figure 3.1. The end-edge depends on the slot coolant flow for protection against in-service erosion.

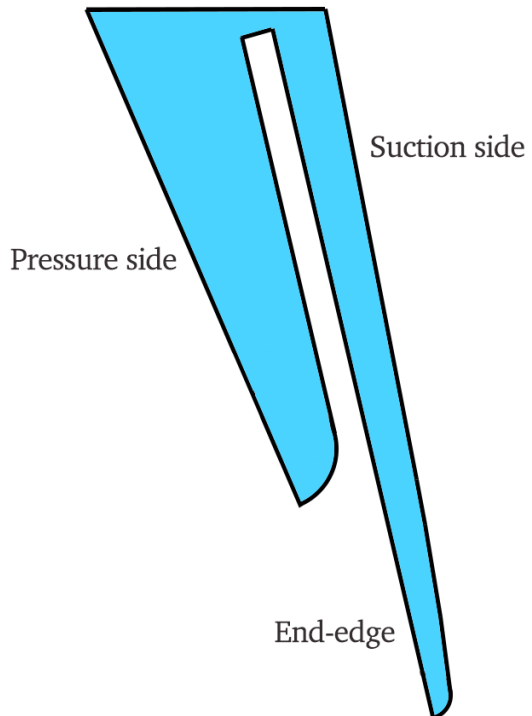


Figure 3.1: Main features of Trent nozzle guide vane trailing edge

The 3-dimensional design of Trent nozzle guide vanes features a transition to allow the end-edge to cleanly meet the end-walls, and an end-edge chord length that is consistent across its span. The creation of a repeatable minimum geometric area which provides the required turning and flow capacity is a primary objective, but so is generating a vane with minimal loss at the start of its service life. These design goals are not necessarily aligned, and it may be the case that a loss-optimised NGV trailing edge is suboptimal in terms of the design's repeatability or susceptibility to unintended changes while in service.

The trailing edge is the part of the vane most susceptible to in-service departures from its build design because it is vulnerable to both cooling and aerodynamic damage. The NGV remains largely intact over its lifetime despite the external gas temperature and high speed external flow. In contrast, the end-edge is subject to significant erosion. If there is a blockage in any of the plena which feed the trailing edge slot, part of its span will receive reduced coolant flow, accelerating the oxidation degradation of the end-edge in that region. Such cooling failures are not uncommon in sandy environments. In such environments, film cooling holes on the pressure side are particularly vulnerable to damage, and this has lead to the adoption of the “cut-back” trailing edge, where the trailing edge region is protected by coolant from the trailing edge slot that is shielded from the mainstream flow to prevent blockage. The pay-off is that the end-edge is now cooled by an external film which must remain attached and is subject to entrainment from the mainstream flow.

The nozzle guide vane must provide a repeatable setting for engine core flow capacity, correct flow turning, and minimal loss. This chapter will predict and analyse these metrics for cases where the shape of the trailing edge is subject to variation. Variations will include incremental reduction in the end-edge length associated with in-service erosion, and incremental reduction in the pressure-side cut-back length as a design variable. The first section of this chapter will review the literature on various definitions of loss, which provides a key measure of performance.

3.1 Definitions of loss for trailing edge performance evaluation

Loss may refer to any process whereby the recoverable energy of a turbomachinery flow is reduced during transit through a turbine stage, other than by shaft work, with corresponding entropy creation. Minimisation of loss remains a primary objective of turbomachinery design, but there is not a universal consensus on how to quantify it. As subsequent sections of this thesis will evaluate the losses caused by changes to the trailing edge of nozzle guide vanes, the purpose of this section is to review various definitions of loss from the literature and to facilitate the use of appropriate definitions in the present study.

Daniel Back da Trinidade et al [9] characterised sources of loss as shock loss, profile losses, tip leakage, endwall losses, and cooling losses. Tip leakage results from flow through the clearance space between the vane tips and the casing. It will not be considered by the present study, since the present study is of fixed NGVs. Endwall losses result from 3-dimensional secondary flows, and will not be considered in the present study which is of 2-dimensional phenomena.

Trinidade et al characterised shock loss as resulting from entropy creation across the shock wave during supersonic flow. The present study will consider this mechanism during discussion of CFD results at choking pressure ratios.

Profile loss was characterised by entropy creation by viscosity in the boundary layer on the blade surface. Entropy generated near the blade's trailing edge was considered as profile loss due to the high entropy creation in the wake region following flow separation at the trailing edge. The authors extended this definition to include the entropy generated as the flow turns tightly around the trailing edge curvature and forms expansion waves.

The authors also defined the category of cooling losses to refer to the aerodynamic penalties incurred by cooling in general, namely “thicker blade profiles from coolant holes, interaction of coolant film with the blade boundary layer, mixing losses between coolant and main flow and endwall losses.” The present study seeks to isolate the mechanisms whereby film cooling causes boundary layer changes and mixing effects, discussing film cooling in Chapter 4.

The present study seeks to define a coefficient of NGV total pressure loss whose arguments are flow measurements or numerically predicted parameters. It is first useful to consider the motivation for quantifying loss in terms of total pressure. This approach treats the nozzle guide vane problem analogously to the problem of flow in a rough pipe, where frictional forces must be balanced by a negative total pressure gradient in the downstream direction. The greater the sum of frictional forces, the greater the loss of total pressure between the inlet and outlet. Total pressure loss can thus aggregate all aerodynamic drag forces acting on the nozzle guide vane or other component.

In an experimental or computational domain, the total pressure loss between inlet and outlet is $p_{01} - p_{02}$. It is intuitive to normalise this against the upstream total pressure p_{01} but it is more useful to normalise it against $p_{01} - p_2$, where p_2 is the outlet static pressure. p_{02} never assumes a value greater than p_{01} or less than p_2 , so if a total pressure loss coefficient is quantified as

$$C_{pt} = \frac{p_{01} - p_{02}}{p_{01} - p_2} \quad (3.1)$$

then the coefficient will be 0 in the case of no total pressure loss, and 1 in the extreme case of $p_{02} = p_2$.

Paul W. Giel et al [10], whose findings will be discussed in Section 3.3, surveyed the total pressure wake profiles of a blade at mid-span. They defined a total pressure loss coefficient as in equation 3.1,

where p_{01} and p_{02} were the inlet and wake total pressures, and p_2 was the wake static pressure.

Jie Gao et al [11], whose findings will be discussed in section 3.2, defined a total pressure loss coefficient as

$$C_{Gao} = \frac{p_{01} - p_{02}}{p_{02} - p_2} \quad (3.2)$$

This definition is equivalent to normalising the total pressure loss against the downstream dynamic pressure. In the case of simulations where the boundary conditions p_{01} and p_2 are set, NGV geometry is the independent variable and p_{02} is the dependent variable. It is thus less convenient for the present study to use Gao et al's loss coefficient formulation, since it does not scale linearly across a range of p_{02} . The definition in equation 3.1 will be used for this reason.

Where subsequent sections are to compare the findings of Giel et al, Gao et al, and other studies of loss, it is required to formulate the total pressure loss coefficient consistently. Gao's definition of C_{pt} may be expanded by Taylor series on the constant p_{01} and as a function of p_{02} as

$$f(p_{02}) = f(p_{01}) + f'(p_{01})(p_{02} - p_{01}) + \frac{1}{2!}f''(p_{01})(p_{02} - p_{01})^2 + \dots \quad (3.3)$$

where $f^n(p_{01})$ may be shown by differentiation to be

$$f^n(p_{01}) = \frac{(-1)^n n!}{(p_{01} - p_2)^n} \quad (3.4)$$

This results in the following mappings between the two definitions of total pressure loss coefficient.

$$C_{Gao} = \sum_{n=1}^{\infty} C_{pt}^n \quad (3.5)$$

$$C_{pt} = \sum_{n=1}^{\infty} (-1)^{n-1} C_{Gao}^n \quad (3.6)$$

Since the total pressure loss coefficient quantifies loss as a summation of all drag forces on the NGV, loss may also be quantified as the total amount of kinetic energy dissipated between inlet and outlet, of the form

$$\zeta = \frac{KE_1 - KE_2}{KE_1} = 1 - \frac{KE_2}{KE_1} \quad (3.7)$$

Kinetic energy may be formulated using the compressible form of Bernoulli's equation as

$$v = \sqrt{2 \left(\frac{\gamma}{\gamma-1} \right) \left[\frac{p_0}{\rho_0} - \frac{p}{\rho} \right]} \quad (1.9)$$

$$v = \sqrt{2 \left(\frac{\gamma}{\gamma-1} \right) RT_0 \left[1 - \left(\frac{p_0}{p} \right)^{\frac{1-\gamma}{\gamma}} \right]} \quad (3.8)$$

The flow's kinetic energy at a given station is thus of the form

$$KE(p) \sim 1 - \left(\frac{p_0}{p} \right)^{\frac{1-\gamma}{\gamma}} \quad (3.9)$$

allowing equation 3.7 to be written as

$$\zeta = 1 - \frac{1 - \left(\frac{p_{02}}{p_2}\right)^{\frac{1-\gamma}{\gamma}}}{1 - \left(\frac{p_{01}}{p_2}\right)^{\frac{1-\gamma}{\gamma}}} \quad (3.10)$$

$$\zeta = \frac{\left(\frac{p_{01}}{p_{02}}\right)^{\frac{\gamma-1}{\gamma}} - 1}{\left(\frac{p_{01}}{p_2}\right)^{\frac{\gamma-1}{\gamma}} - 1} \quad (3.11)$$

This definition of kinetic energy loss coefficient was used by Giel et al. Like the total pressure loss coefficient, it takes a value of 0 in the case of no loss where $p_{02} = p_{01}$, and 1 in the extreme case of $p_{02} = p_2$.

Ranjan Saha et al [12] experimentally investigated the loss effects of shower-head and trailing edge cooling in an annular sector. By defining kinetic energy loss in 3 alternative ways, the authors demonstrated the extent to which computed loss can vary depending on definition. Discrepancies were shown to result from how the coolant kinetic energy is accounted for. Where the ratio of coolant mass flow rate to mainstream mass flow rate was Y , the authors defined kinetic energy loss as

$$\zeta = 1 - \frac{(1+Y) \left[1 - \left(\frac{p_2}{p_{02}} \right)^{\frac{\gamma-1}{\gamma}} \right]}{\left[1 - \left(\frac{p_2}{p_{01}} \right)^{\frac{\gamma-1}{\gamma}} \right] + Y \left[1 - \left(\frac{p_2}{p_{0c}} \right)^{\frac{\gamma-1}{\gamma}} \right]} \quad (3.12)$$

In the case of no coolant flow ($Y = 0$) this is equivalent to the definition in equation 3.11. Equation 3.12 is equivalent to the loss definition defined by Mathias Deckers and John D. Denton [13] in the case of no significant temperature difference between coolant and mainstream, as in a significant proportion of experimental studies.

Where coolant flow is present, equation 3.12 requires a local value of Y in order to obtain the loss at any particular point. Assuming that the coolant concentration is a function of the local total pressure loss compared to an uncooled vane, the authors redefined Y as a function of spanwise distance x as

$$\frac{Y(x)}{Y_{max}} = \frac{p_{02uc} - p_{02}(x)}{|p_{02uc} - p_{02}|_{max}} \quad (3.13)$$

where p_{02uc} was the total pressure downstream of the cascade with no cooling, p_{02} was the total pressure downstream of the cascade as a function of spanwise distance (with cooling), and $|p_{02uc} - p_{02}|_{max}$ denotes the maximum possible difference in downstream total pressure between the uncooled and the cooled cases. Reasoning that this total pressure difference is maximal when $p_{02} = p_{01}$ and $p_{02} = p_{wake}$ (the total pressure in the wake region), Saha et al thus defined their function for local coolant/mainstream mass flux ratio as

$$\frac{Y(x)}{Y} = \frac{p_{02uc} - p_{02}(x)}{p_1 - p_{02wake}} \quad (3.14)$$

By substituting this definition of Y into equation 3.12, Saha et al arrived at their novel definition of kinetic energy loss intended to solve the problem of unphysical loss in the free-stream where the previous definition erroneously assumed the presence of coolant. Their new definition is able to use the nominal values for shower-head and trailing edge coolant mass flow ratio and adjust the coolant profile according to the aforementioned function of spanwise distance. Using measurements from a downstream traverse in their linear cascade, the novel loss definition was found to produce loss profiles that were in good agreement with equation 3.11 and in disagreement with equation 3.12.

3.2 Effects of suction-side trailing edge shape uncertainty

This section will consider increasingly severe loss of material up to a potential worst case for in-service erosion of the end-edge, namely its complete deletion. Erosion has been assumed to take place at the NGV mid-span where flow speeds and temperatures are highest and there is evidence of in-service damage. Here secondary flows across the blade are small and a 2-dimensional simulation of the mid-span flow should provide a physically realistic measure of performance.

3.2.1 Geometry, mesh, and boundary conditions

2D CFD has been used to model the effects of incremental removal of material from the suction-side end-edge of an NGV. The baseline geometry is vane KSZ03 from the 6 vanes provided by Rolls-Royce for the work discussed in Chapter 2. The 2D vane section was produced using the process illustrated in Figure 2.2. The overall computational domain was produced as in Figure 2.3. Unlike the section of vane KSZ03 studied in Chapter 2, the NGV trailing edge was not rounded but realistically shaped, and the domain was modified to include a flow inlet within the NGV's trailing edge slot, where inlet mass flow rate was specified. The boundary conditions used for all simulations are as listed in Table 3.1.

Simulations were performed at a range of inverse pressure ratios between 1.5 and 3.33, and particular study was made at inverse pressure ratios of 1.5, 1.79 and 3.33. This permits comment on the NGV flow capacity as a function of only the sonic line shape, and eliminates the possibility of unchoked flow passing through the nozzle, with the exception of the boundary layers. $\frac{p_{01}}{p_2} = 3.33$ was considered to be a case where the nozzle guide vane is definitely fully choked. Although this particularly high inverse pressure ratio is possibly unachievable in the real engine, the simulated NGVs were observed to be fully choked at a substantially lower inverse pressure ratio of 2.5. $\frac{p_{01}}{p_2} = 1.79$ is the design cruise condition for the Trent 900 engine. $\frac{p_{01}}{p_2} = 1.5$ was considered to be a case where the nozzle guide vane is definitely not choked, and is possible to achieve in some very low-power operating conditions.

Table 3.1: Boundary conditions for end-edge shape uncertainty study

Parameter	Value
NGV series	Rolls-Royce Trent 900
NGV turning (degrees)	76.89
Inverse pressure ratio $\frac{p_{01}}{p_2}$	1.5, 1.79, 3.33
Inlet total pressure (Pa)	4.33×10^6
Inlet total temperature (K)	300
Outlet static pressure (design) (Pa)	2.42×10^6
Outlet static temperature (Pa)	300
Coolant mass flow rate	3% of mainstream
Solver type	Density-based
Cell count	35,000

The strategy for geometry alteration and meshing was to divide the geometry into quadrilateral regions of solid vane that were sequentially replaced by regions of fluid mesh. Each replacement incrementally eroded or cut back the NGV's end-edge. This required minor alteration of the trailing

edge geometry provided by Rolls-Royce. The curved surface on the inside of the pressure side was changed to a straight line with an angular corner, and the curved tip of the suction side was changed to a square end. Comparison of the shape of manufactured NGVs with the shape of design-intent NGVs demonstrates that the present study's trailing edge treatment is more reflective of the manufactured NGVs, which have corners rather than smooth curves in the places in question. In any case the radius of curvature of the corner is too sharp to promote any attachment of the internal flow over its length, and so is aerodynamically irrelevant. The process of geometry refinement and incremental mesh block creation is illustrated in Figure 3.2.

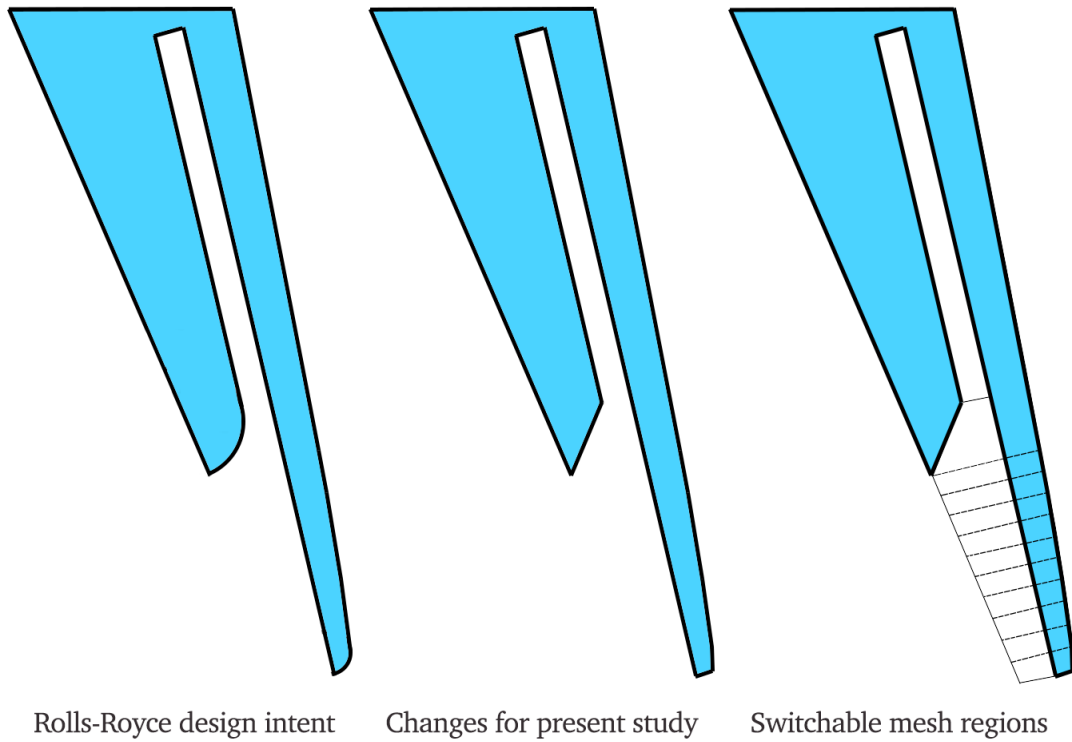


Figure 3.2: Geometry processing scheme for cutbacks to the end-edge of a Trent 900 NGV

The resulting quadrilateral geometry allowed for the creation of a structured mesh that could be matched with a structured boundary layer mesh of the same design as that depicted in Figure 2.5b. Beyond this, an unstructured mesh was created to the same design as that depicted in Figure 2.4. Detail of the trailing edge mesh is shown in Figure 3.3 for a case where approximately 50% of the end-edge is removed and replaced with structured fluid mesh blocks.

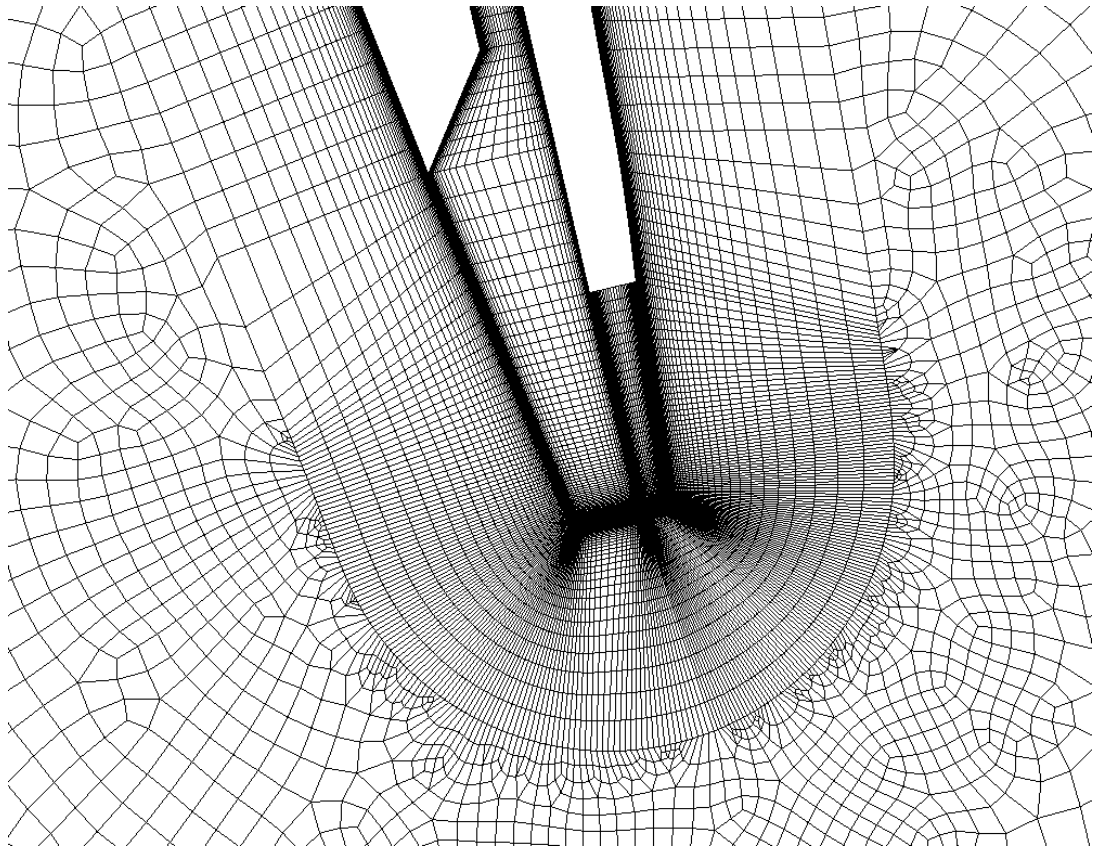


Figure 3.3: Example of mesh for cutbacks to the end-edge of a Trent 900 NGV

The described mesh, geometry alteration strategy, and boundary conditions were used to perform 11 CFD simulations which incrementally spanned the range of cutbacks between an unaltered trailing edge and a fully removed end-edge. Solutions were initialised using the solver's built-in FMG initialisation and Journal scripts as described in Section 2.1. NGV mass flow rate was saved at each pressure ratio. Full solution data were saved for the final fully choked pressure ratio to enable analysis of the shocks, expansions and sonic line at choked conditions. There were 32 increments and typical overall solution times were approximately 10 hours. The SST- $k\omega$ turbulence model was used.

3.2.2 Effect on capacity

Figure 3.4 shows contours of Mach number in the region of the trailing edge for the described study. The depicted range of cutbacks is between the unaltered baseline and the case of 30% removal of the overall length of the suction-side end-edge. Inverse pressure ratio is 3.3, fully choked.

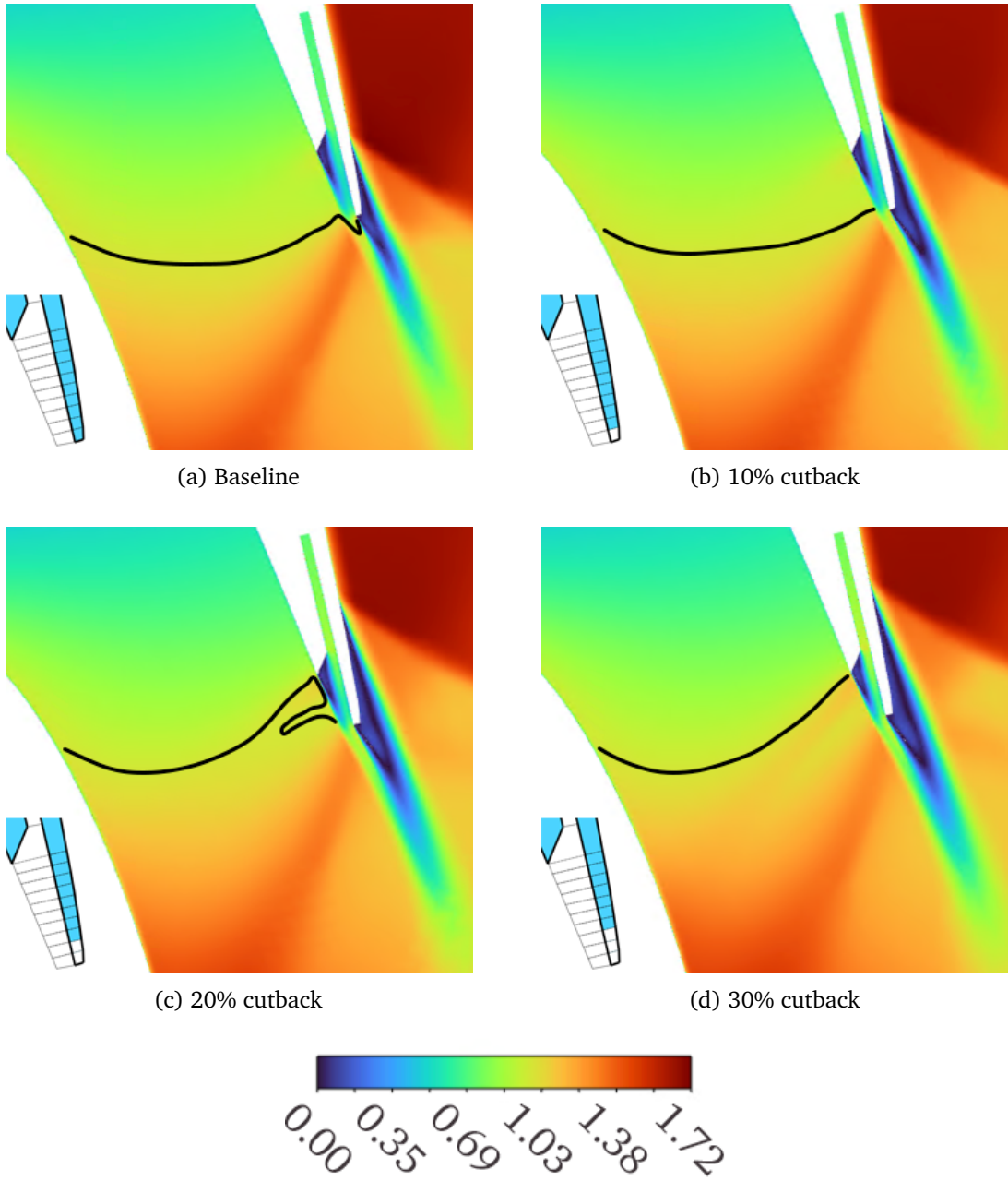


Figure 3.4: Effects of small cutbacks on sonic line shape for Trent 900 end-edge erosion study at $\frac{p_{01}}{p_2} = 3.33$

Figure 3.4 illustrates the subtle changes in the sonic line at the nozzle exit as the nozzle guide vane's end-edge is incrementally removed until 30% of its length is not present. The sonic line is shown to undergo a fundamental transition over this range of cutbacks, from initially impinging on the extremity of the end-edge in the baseline case, to impinging on the acute corner of the pressure side. The geometric changes are also shown to alter the aerodynamics in the suction-side region upstream of the end-edge, where an attached shock moves incrementally upstream with each increment in cutback. Shock-induced boundary layer separation is seen to be present in Figure 3.4, and moves upstream corresponding to the position of the shock. This results in an increasingly large separated wake region which is not in alignment with the NGV's turning angle.

Figure 3.5 shows contours of Mach number in the region of the trailing edge for the described study.

The depicted range of cutbacks is between the case of 40% and the case of complete removal of the end-edge. Inverse pressure ratio is 3.3, fully choked.

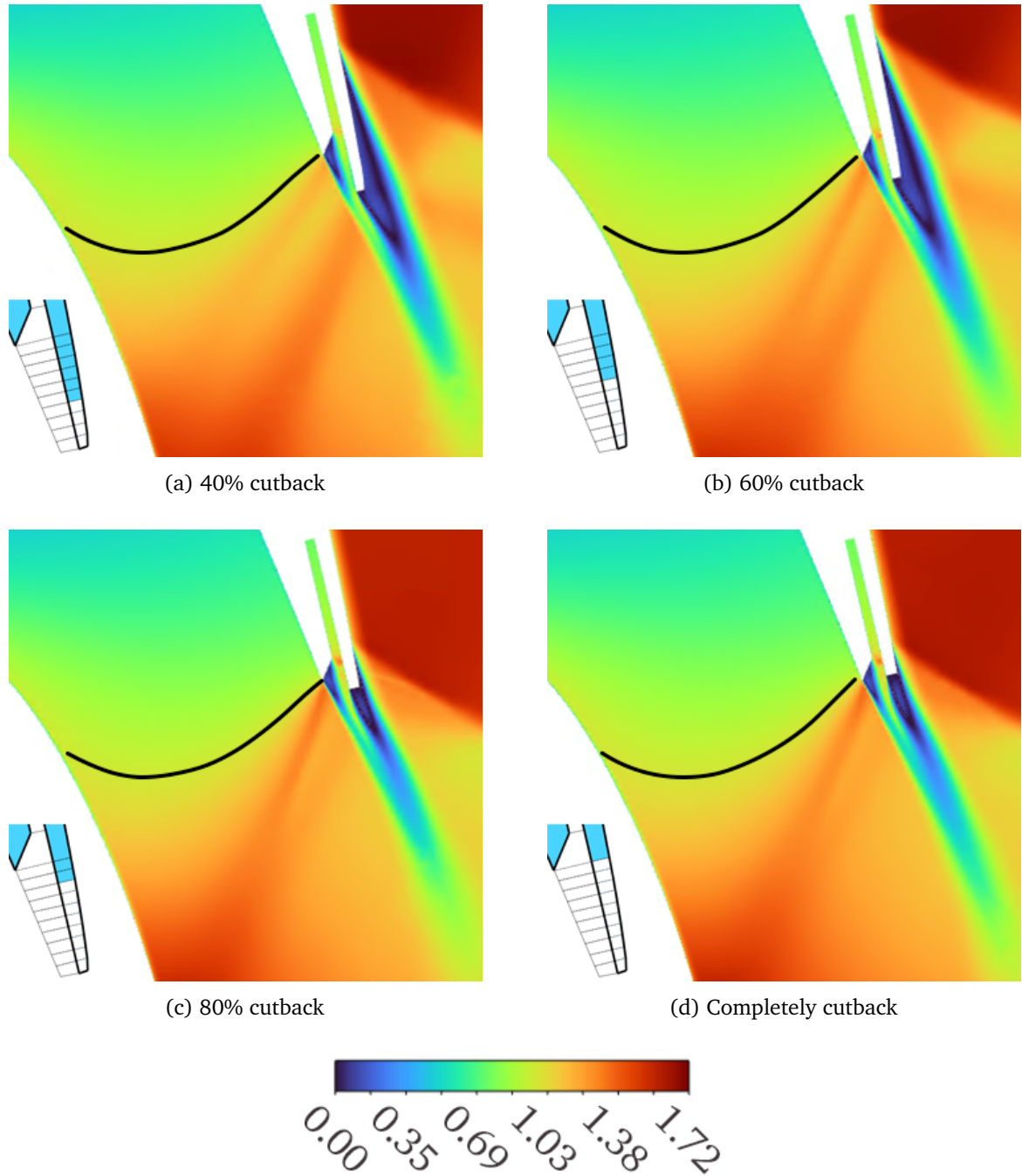


Figure 3.5: Effects of large cutbacks on sonic line shape for Trent 900 end-edge erosion study at $\frac{p_{01}}{p_2} = 3.33$

Figure 3.5 illustrates that the shape of the sonic line is not fundamentally altered in the range between 40% and 100% removal of the end-edge. The sonic line is shown to consistently attach to the acute corner of the pressure side throughout this range of larger cutbacks. Upstream movement of the location of the suction-side attached shock continued to occur. This trend was reversed for the most extreme cases of 80% and complete cutbacks, where the shock transitioned to a downstream location close to the corner of the end-edge, resulting in a significantly smaller separated wake region

compared to other cases.

The set of Mach number contours and sonic lines suggest that the greatest sensitivity of flow capacity to end-edge cutbacks is to occur for cutbacks of 30% of the end-edge or less. The sensitivity of the sonic line shape to the full range of cutbacks is illustrated in Figure 3.6. It is further suggested that the location of an attached shock and corresponding boundary layer separation may be sensitive to cutbacks of 40% or more, but this may be imprecisely predicted by the present simulations.

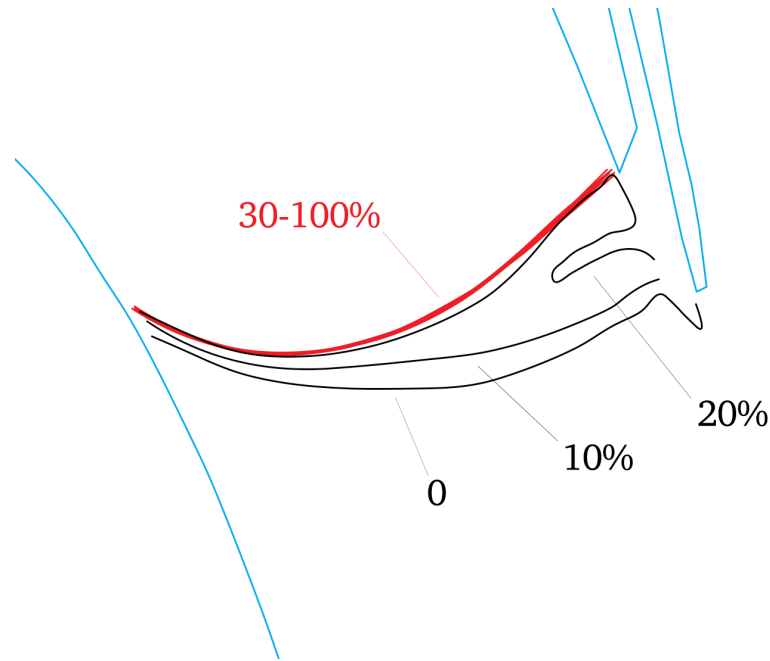


Figure 3.6: Effects of full range of cutbacks on sonic line shape for Trent 900 end-edge erosion study, labelled by 10% of end-edge removed

Figure 3.6 shows that upstream movement of the location of the suction-side attached shock occurred between 0 and 30% removal of the end-edge. This trend did not continue for cutbacks greater than 30%.

Figure 3.7 plots flow capacity change as a function of the amount of the end-edge that has been removed. The trend is plotted for 3 inverse pressure ratios: 1.50, the design value of 1.79, and a fully choked value of 3.33.

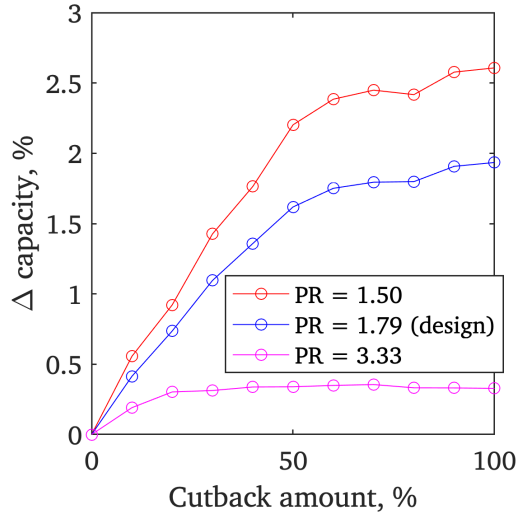


Figure 3.7: 2D capacity percentage delta as a function of end-edge cutback amount for 3 pressure ratios

At an inverse pressure ratio of 3.33, Figure 3.7 shows a relationship between flow capacity and cutback amount which is in good agreement with the observations made from the corresponding sonic line visualisations. Capacity is shown to be sensitive to cutback amounts of 0, 10%, and 20%, and insensitive to cutbacks thereafter. The corresponding sonic lines are observed to vary in shape when capacity varies, and to remain similar in shape when capacity does not vary. The observed switching of the sonic line from the end-edge-attached mode (at baseline) to the pressure-side-attached mode (at cutbacks of 30% and greater) is associated with a 0.3 percentage point increase in capacity. For all cutbacks subsequent to the mode switch, there is no capacity change at this pressure ratio. This is in good agreement with the discussion in Chapter 2 which concluded that the effective throat area of a fully choked nozzle guide vane is predominantly a function of the shape of its sonic line.

At lower inverse pressure ratios where the flow is not fully choked, and thus a sonic line cannot be drawn, flow capacity varied over a significantly greater range of cutback percentage. This is to be expected by consideration of choked versus unchoked compressible flows as discussed earlier in this section. This discussion implies that, in the general case of compressible flow in 2D nozzles, the nozzle flow capacity will increase if the effective passage width is increased at any point along the nozzle. However, this is also a consequence of providing less turning in the flow. An entirely unturned flow would have maximum capacity in the annular cross-section that is the gas turbine.

This is in good agreement with the observed relationship between flow capacity and cutback amount at the unchoked pressure ratios. Removal of end-edge material increases the effective passage width in the region local to the end-edge, causing a local decrease in static pressure and increase in dynamic pressure. Because most streamlines are unchoked at the flow region and pressure ratios in question, this state change propagates along the entire streamline with a corresponding increase in mass flow rate.

The maximum change in capacity was 1.9 percentage points at the design inverse pressure ratio of 1.79, and 2.5 percentage points at an inverse pressure ratio of 1.50. The effect of increasing cutbacks became less pronounced at larger cutback amounts, suggesting that the size of the end-edge ceases to be the limiting factor on effective passage width for those geometries. Figure 3.8 shows contours of Mach number in the NGV wake region for the full range of cutbacks at the design inverse pressure

ratio of 1.79.

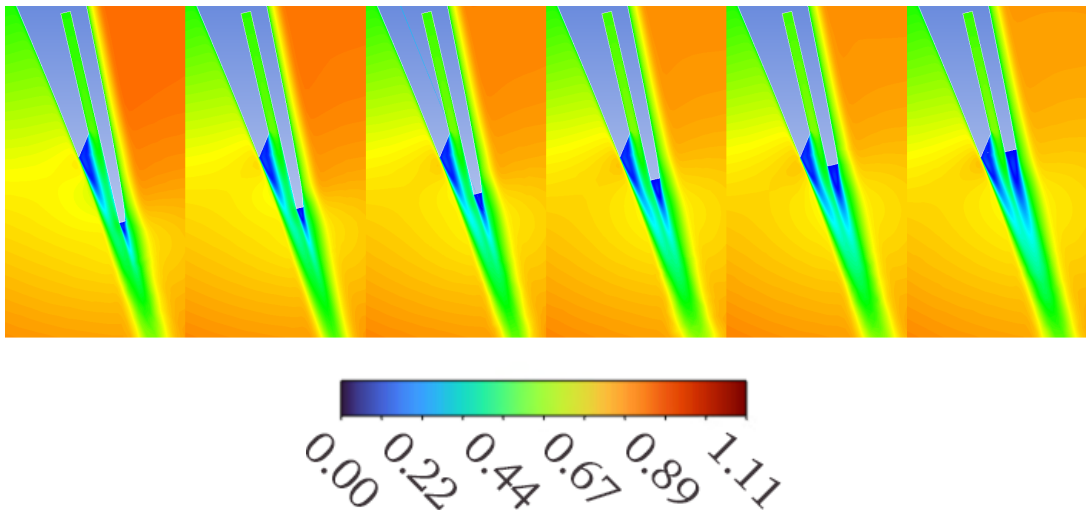


Figure 3.8: Contours of Mach number in the wake region of the Trent 900 end-edge erosion study at $\frac{P_{01}}{P_2} = 1.79$ (design)

Key features of Figure 3.8 include an outer wake region (rendered in green) and inner wake regions downstream of the pressure side and the end-edge (rendered in blue). No fundamental changes occurred to the trailing edge's aerodynamics over the range of cutbacks. Mach number is observed to continually increase in the region adjacent to the pressure side, and to continually decrease in the region adjacent to the end-edge. The trailing edge aerodynamics were sensitive to geometric changes across the full range of cutbacks. The reduced effect of greater cutbacks on flow capacity may result from two phenomena. Firstly, the local flow acceleration may be limited more by the position of the pressure side than by the end-edge at higher cutback values, where the end-edge tip is increasingly too far upstream to influence the pressure-side aerodynamics. Secondly, this upstream positioning of the end-edge tip is observed to cause a significant increase in outer wake thickness at higher cutback values. This likely reduced the effective passage width in this region and counteracted the predominant effect of flow capacity increasing.

Figure 3.9 plots trends of flow capacity change versus inverse pressure ratio at selected cutback amounts. The range of inverse pressure ratios includes the design value of 1.79.

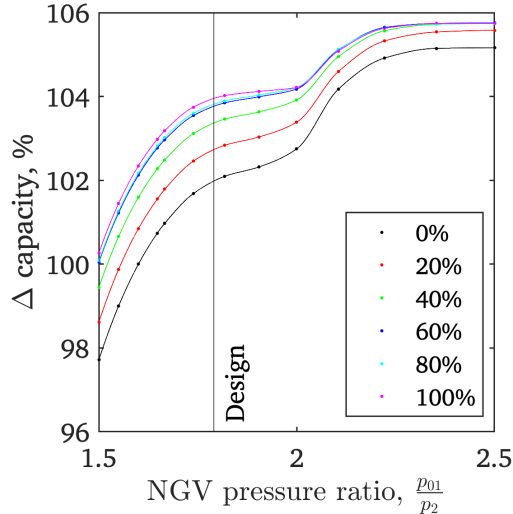


Figure 3.9: 2D capacity trends for various end-edge cutback amounts

In terms of the effects of cutbacks on flow capacity, Figure 3.9 is in good agreement with Figure 3.7. The capacity delta produced by full end-edge removal continuously decreased with increasing inverse pressure ratio, and the capacity trends remained qualitatively similar for all cutback amounts. These observations suggest that the cutback-induced capacity changes and the onset of choking are 2 independent phenomena which do not influence each other. It is concluded that, as inverse pressure ratio increased, more streamlines became choked and ceased to be affected by cutbacks downstream of those streamlines' sonic points.

It is further concluded that the capacity trend shapes and onsets of choking were unaffected by variable cutbacks, but remained a function of only inverse pressure ratio. This is likely due to the relevant geometric changes taking place downstream of the throat region. This is complementary to the results of Chapter 2, where geometric changes upstream of the throat resulted in qualitatively distinct capacity trends and dissimilar onsets of choking.

3.2.3 Effect on performance

Simulation data were also used to evaluate the aerodynamic penalties associated with the incremental cutbacks to the end-edge at the design inverse pressure ratio of 1.79. These penalties include the change to the NGV's ability to turn the flow by the correct angle, and the effect of the cutbacks on the NGV loss.

Velocity components at the domain outlet were surveyed and averaged over the length of the outlet. This resulted in a value for mean NGV turning angle for each incremental cutback. Figure 3.10 plots turning angle deviation in degrees versus end-edge cutback amount.

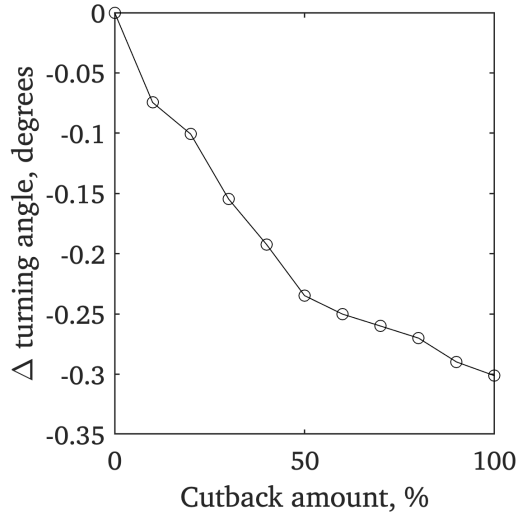


Figure 3.10: NGV turning angle delta as a function of end-edge cutback amount at $\frac{p_{01}}{p_2} = 1.79$

Figure 3.10 shows that the NGV's ability to turn the flow was significantly reduced as cutbacks increased. Complete removal of the end-edge resulted in a turning angle reduction of 0.3 degrees, with increased sensitivity to cutbacks at smaller cutback amounts. This trend is in agreement with the extreme scenario of having no vane at all, where there would correspondingly be no turning at all.

Overall flow turning angle was surveyed along the length of the domain outlet plane. Figure 3.11 plots this distribution of turning angles at selected cutback amounts. On the outlet plane, $0 \rightarrow 1$ denotes travel in the negative y direction, which is the direction the flow turns. Stations 0 and 1 are labelled on the illustration of the computational domain in Chapter 2, Figure 2.3.

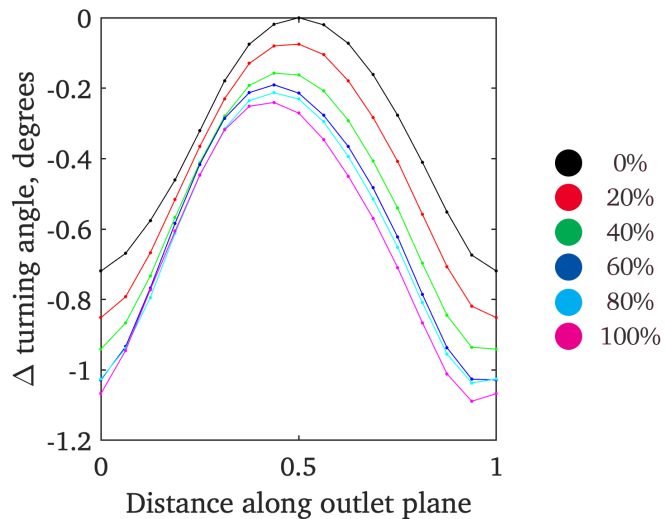


Figure 3.11: Outlet plane turning angle surveys for various end-edge cutback amounts at $\frac{p_{01}}{p_2} = 1.79$

Figure 3.11 further illustrates the trend of reducing turning angles present in Figure 3.10. It is also apparent that the incremental cutbacks caused a shift in the location of maximum turning angle. In the case of no cutback, maximum turning occurred exactly halfway across the domain exit plane, at a location immediately downstream of the NGV end-edge. Subsequent cutbacks caused both a

reduction in maximum turning and a shift of the maximum turning location in the opposite direction to which turning occurs. This suggests that the NGV wake continued to extend downstream of the NGV at an angle which decreased with increasing cutbacks, arriving at the domain outlet at an incrementally increasing y -coordinate. Assuming that the downstream turning angle distribution is indicative of the NGV wake profile, the wake did not appear to become significantly more diffuse as cutbacks increased.

Figure 3.12 plots loss as a function of end-edge cutback amount at the design pressure ratio of 1.79, where total pressure loss and kinetic energy loss are defined as in Section 3.1. Total pressure values were surveyed at the domain outlet plane and averaged to produce the loss values.

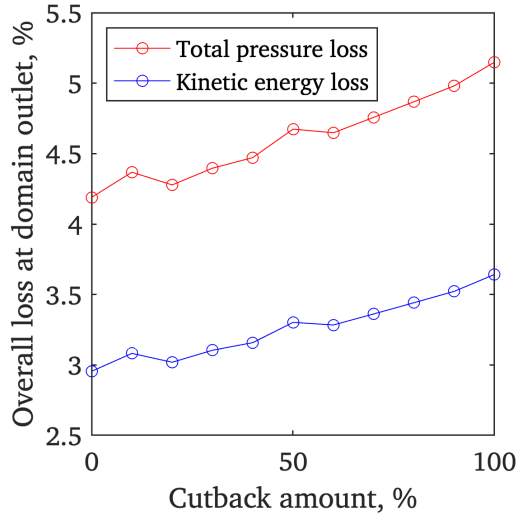


Figure 3.12: Loss as a function of end-edge cutback amount at $\frac{p_{01}}{p_2} = 1.79$

Figure 3.12 shows that both types of loss increased with incremental cutbacks. Total pressure loss was observed to increase by approximately 1% over the range of cutbacks, and kinetic energy loss by approximately 0.7%. This is in agreement with the discussion of figure 3.8 which suggested that loss would likely be incurred by the increasing area of separated wake that occurs as cutbacks increase. This effect may be exacerbated by the deviation from the design turning angle that also occurs, whereby the NGV wake is deflected in the positive x -coordinate with corresponding increase in its area.

Loss delta is plotted as a function of capacity delta in Figure 3.13. This plot covers the range of incremental cutbacks and is for the design inverse pressure ratio of 1.79.

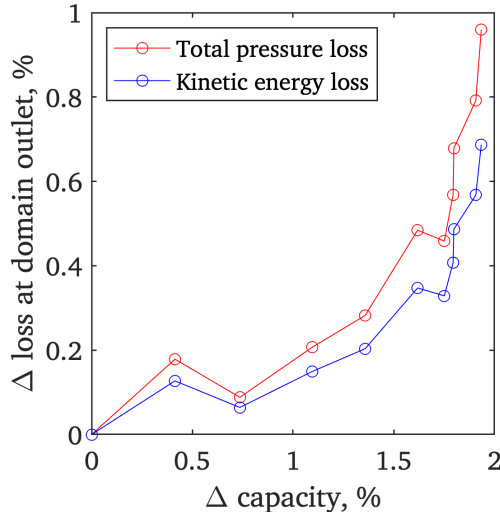


Figure 3.13: Loss delta as a function of capacity delta for end-edge cutbacks at $\frac{P_{01}}{P_2} = 1.79$

Figure 3.13 shows that, as the end-edge is incrementally removed, capacity and loss do not change in direct proportion to each other. Although overall capacity sensitivity was greater than overall loss sensitivity, at higher cutback amounts a relatively small increase in capacity corresponded to a sharp increase in loss by both definitions. In agreement with this section's previous analysis of the capacity and loss mechanisms present across the range of cutbacks, it is concluded that capacity sensitivity is of greatest concern in cases of relatively small erosion of the NGV end-edge, and loss sensitivity is of concern in all cases but especially in cases of relatively large erosion.

3.3 Effects of pressure-side trailing edge sizing

This section considers the location of the pressure-side cutback that is present on the NGV. This feature is required to prevent blockage of the coolant supply to the end-edge, which would be damaged very rapidly by oxidation erosion if the slot coolant flow were not present. Although the pressure side could be extended further downstream into a thinner feature with a smaller wake, the cutback prevents blockage of the slot coolant flow by causing it to form an external film attached to the pressure side of the end-edge. If a coolant blockage is present upstream inside the vane, the end-edge coolant film will remain relatively unchanged after mixing with itself.

Improved materials and manufacturing techniques may necessitate alternative trailing edge geometries. Paul W. Giel et al [10] noted that “in the pursuit of higher turbine inlet temperatures for reduced fuel burn and emissions consistent with NASA’s goals [14], Ceramic Matrix Composite (CMC) materials are now being implemented in gas turbine engines...They enable higher turbine inlet temperatures, thus enabling higher overall pressure ratios (OPRs) for the engine and higher thermal efficiency.”

The authors used a linear cascade to measure the aerodynamic performance of a set of blades representing the geometric constraints of the CMC manufacturing method. Of main concern was the constraint that “the trailing edge thicknesses of CMC blades are anticipated to be significantly larger than those of current state-of-the-art metallic blades,” which may be expected to cause increased loss.

3.3.1 Geometry, mesh, and boundary conditions

The larger the pressure-side cutback, the less the likelihood of coolant blockage, and the easier it is to perform the machining of the trailing edge. However, a bigger cutback is expected to cause increased loss due to increased wake area, as well as reduced film cooling effectiveness on the end-edge as the coolant becomes mixed out. This section presents a 2D CFD study on varying the size of the pressure-side cutback, using the types of analyses presented for end-edge cutbacks in Section 3.2. The baseline geometry included a partially eroded end-edge to be representative of the full lifetime of the component, for which a cutback amount of approximately 50% was chosen. The baseline pressure-side cutback was such that the pressure side and the suction side extended by the same amount, with no end-edge. Cutbacks were then made to move the end of the pressure side upstream in increments of 25%, where 100% is equivalent to the existing location of the pressure side of the trailing edge. The process of geometry refinement is illustrated in Figure 3.14.

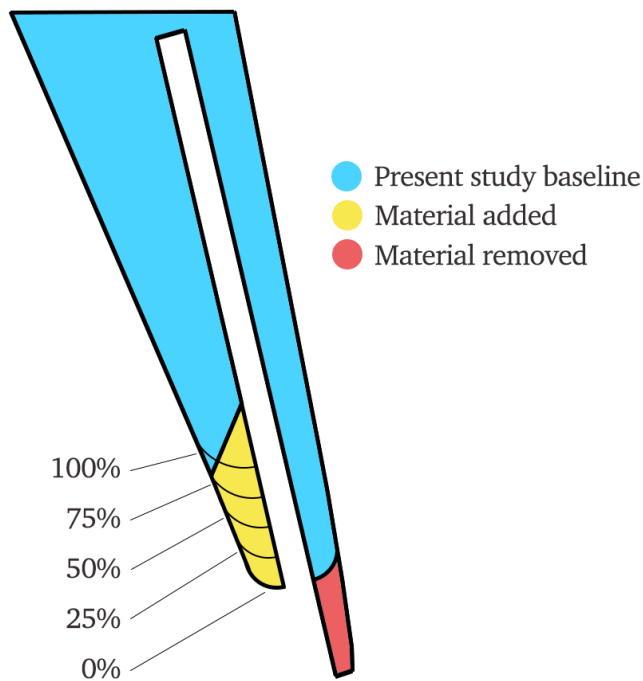


Figure 3.14: Geometry processing scheme for cutbacks to the pressure side of a Trent 900 NGV

As in Section 3.2, simulations were performed at a range of inverse pressure ratios between 1.5 and 3.33, and particular study was made at inverse pressure ratios of 1.5, 1.79 and 3.33. 1.79 is the design cruise condition for the Trent 900 engine. Boundary conditions were as described in Table 3.1.

This geometry did not allow for the approach of Section 3.2 where material was replaced with structured fluid mesh. For this geometry, an additional structured quadrilateral mesh block was created for cutback sizes greater than 0. This block deformed as cutbacks were increased, maintaining element spacing on the outer edge of the structured boundary layer mesh region. The sizing of this region was consistent with that used in Section 3.2, as was the design of the unstructured quadrilateral mesh for the overall domain. Figure 3.15 depicts the meshes used for the cases of 0%, 25%, 50%, and 75% cutbacks.

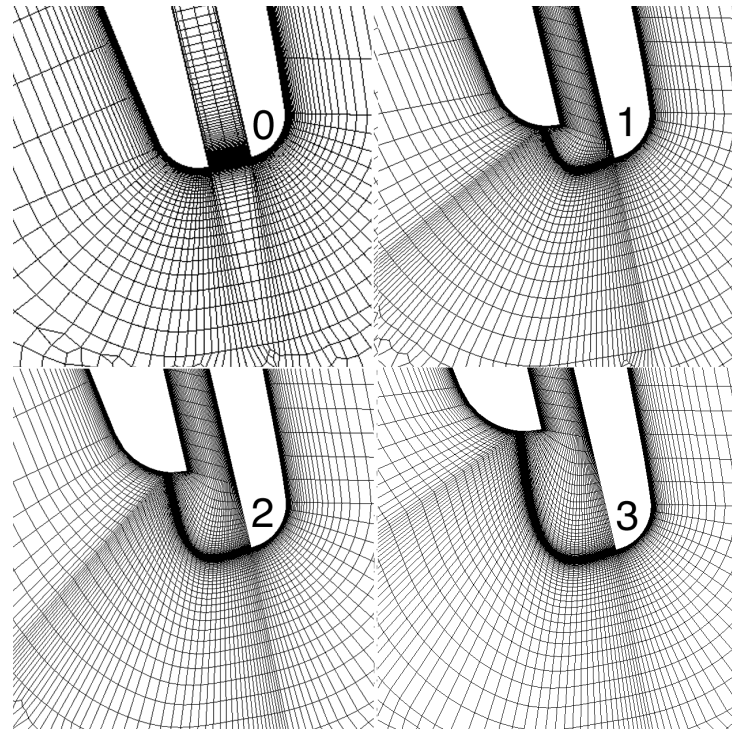


Figure 3.15: Examples of meshes for cutbacks to the pressure side of a Trent 900 NGV

In Figure 3.15, deformation of the bottom edge of the aforementioned mesh block is prominently visible due to the continuation of the laminar sublayer resolution around the circumference of the vane, which requires it to bridge the gap across the trailing edge slot. The described mesh, geometry alteration strategy, and boundary conditions were used to perform 5 CFD simulations which incrementally spanned the range of cutbacks between the described baseline and a fully cut back pressure side. Solutions were initialised using the solver's built-in FMG initialisation and Journal scripts as described in Section 2.1. NGV mass flow rate was saved at each pressure ratio. Full solution data were saved for the final fully choked pressure ratio to enable analysis of the shocks, expansions and sonic line at choked conditions. There were 32 increments and typical overall solution times were approximately 10 hours. The SST- $k\omega$ turbulence model was used.

3.3.2 Effect on capacity

Figure 3.16 shows contours of Mach number in the region of the trailing edge for the described study. The depicted range of cutbacks is between 0% and 100%. Inverse pressure ratio is 3.33, fully choked.

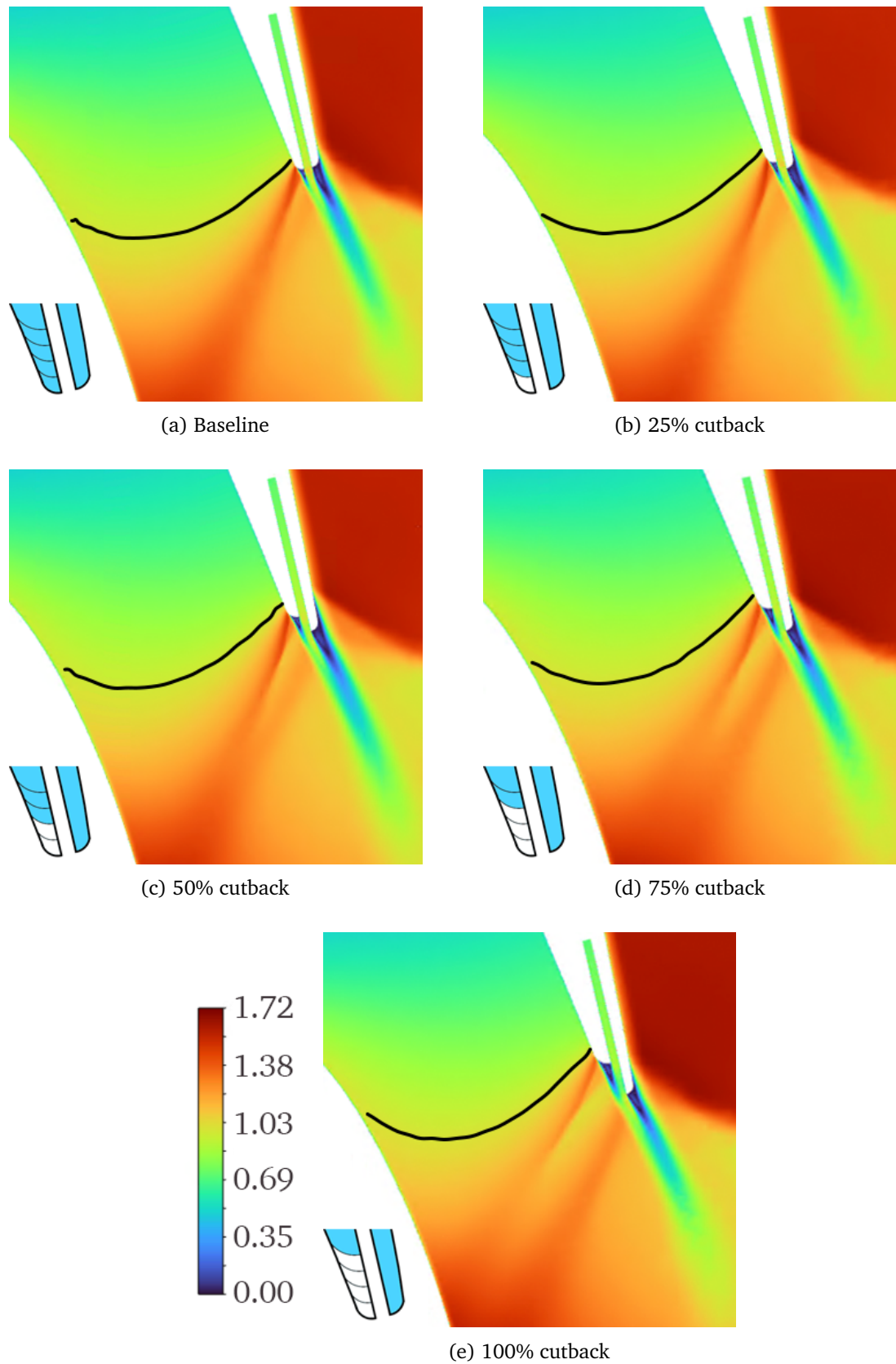


Figure 3.16: Effects of cutbacks on sonic line shape for Trent 900 pressure-side cutback study at $\frac{p_{01}}{p_2} = 3.33$

Figure 3.16 illustrates that the sonic line moved incrementally upstream with increasing pressure-side

cutbacks. The sonic line remained attached to the pressure side of the trailing edge at a point just upstream of where boundary layer separation occurred, and this remained true as both the pressure side and the sonic line progressed upstream as cutbacks increased. On the suction side of the adjacent vane, the sonic line attached at a point that also moved incrementally upstream. In all cases, a shock was present immediately upstream of the point of pressure-side boundary layer separation, which was in a region of high convex curvature on the vane surface. Shock-induced boundary layer separation also occurred on the suction side of the trailing edge at a location that was not affected by the incremental changes to the pressure side. In cases of 25% cutback or more, an additional shock appeared downstream of the pressure-side trailing edge, and appeared stronger as cutbacks increased. The overall trend observed is that increasing cutbacks caused the line of geometric minimum width to move upstream, and that the sonic line moved upstream correspondingly. This observation is supported by the relationship between the cutback amount and the nozzle's geometric throat width, which is plotted in Figure 3.17. The sensitivity of the sonic line shape to the full range of cutbacks is illustrated in Figure 3.18.

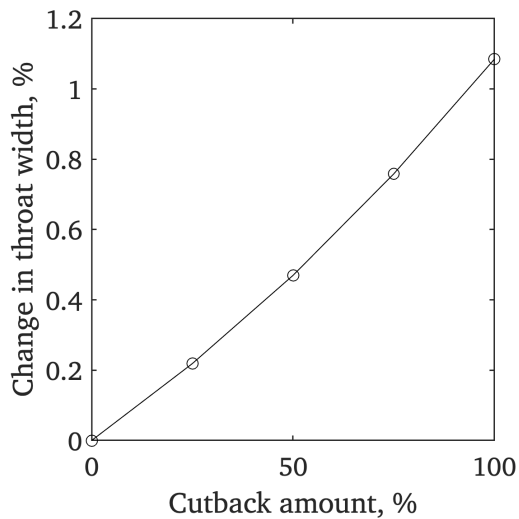


Figure 3.17: NGV geometric throat width as a function of cutback amount

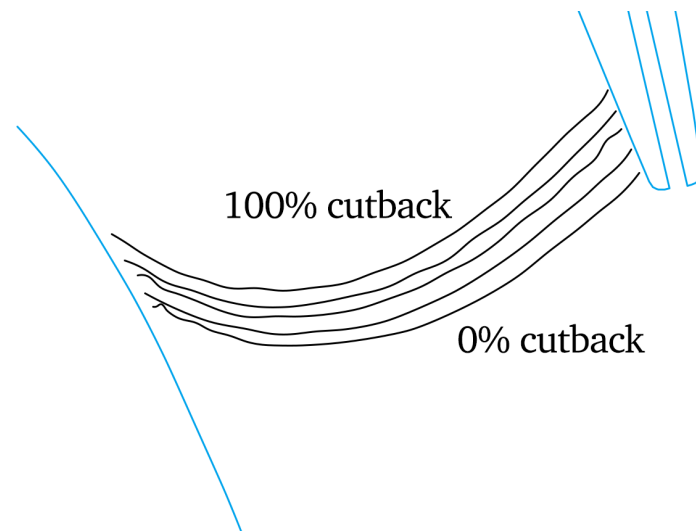


Figure 3.18: Effects of full range of cutbacks on sonic line shape for Trent 900 pressure-side cutbacks study, labelled by % of cutback

Figures 3.17 and 3.18 are in good agreement with the hypothesis that increasing the pressure-side cutbacks resulted in an upstream movement of the NGV's geometric throat line, with a corresponding increase in throat width that was approximately linearly related to the size of the cutback.

Figure 3.19 plots flow capacity change as a function of the amount of pressure-side cutback. The trend is plotted for 3 inverse pressure ratios: 1.50, the design value of 1.79, and a fully choked value of 3.33.

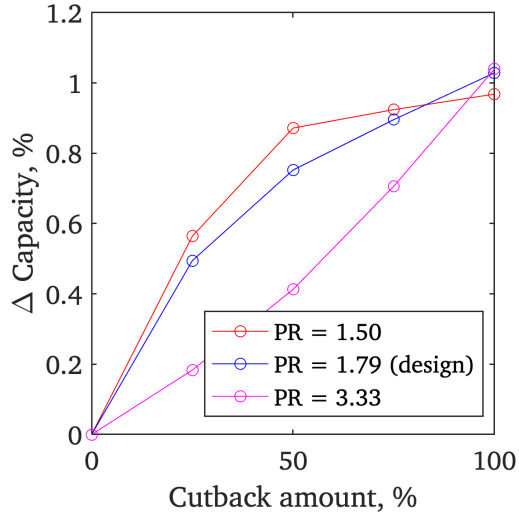


Figure 3.19: 2D capacity percentage delta as a function of pressure-side cutback amount for 3 pressure ratios

At an inverse pressure ratio of 3.33, Figure 3.19 shows a relationship between cutback amount and capacity delta that is in agreement with the hypothesis that the present changes are driven by an incremental increase in throat area. The graph of capacity versus cutback amount is similar in shape to the graph of throat width versus cutback amount in Figure 3.17. At the design inverse pressure ratio, capacity initially increased sharply with cutback amount but became less sensitive for greater cutbacks. At both the fully choked and the design inverse pressure ratios, 100% cutback resulted in a 1% increase in flow capacity. At the unchoked inverse pressure ratio of 1.5, the change in capacity was slightly smaller at 0.97%.

Overall it was apparent that only the fully choked cases were changing in direct proportion to changes to the nozzle throat width, with 100% cutback increasing both throat width and flow capacity by 1%. The design-condition cases and fully unchoked cases were evidently subject to aerodynamic changes downstream of the trailing edge region which allowed for greater sensitivity to smaller cutbacks and lesser sensitivity to larger cutbacks. To illustrate some of the relevant aerodynamic effects, Figure 3.20 shows contours of Mach number in the region of the trailing edge for the described study. The depicted range of cutbacks is between 0% and 100%. Inverse pressure ratio is 1.79, the design cruise condition.

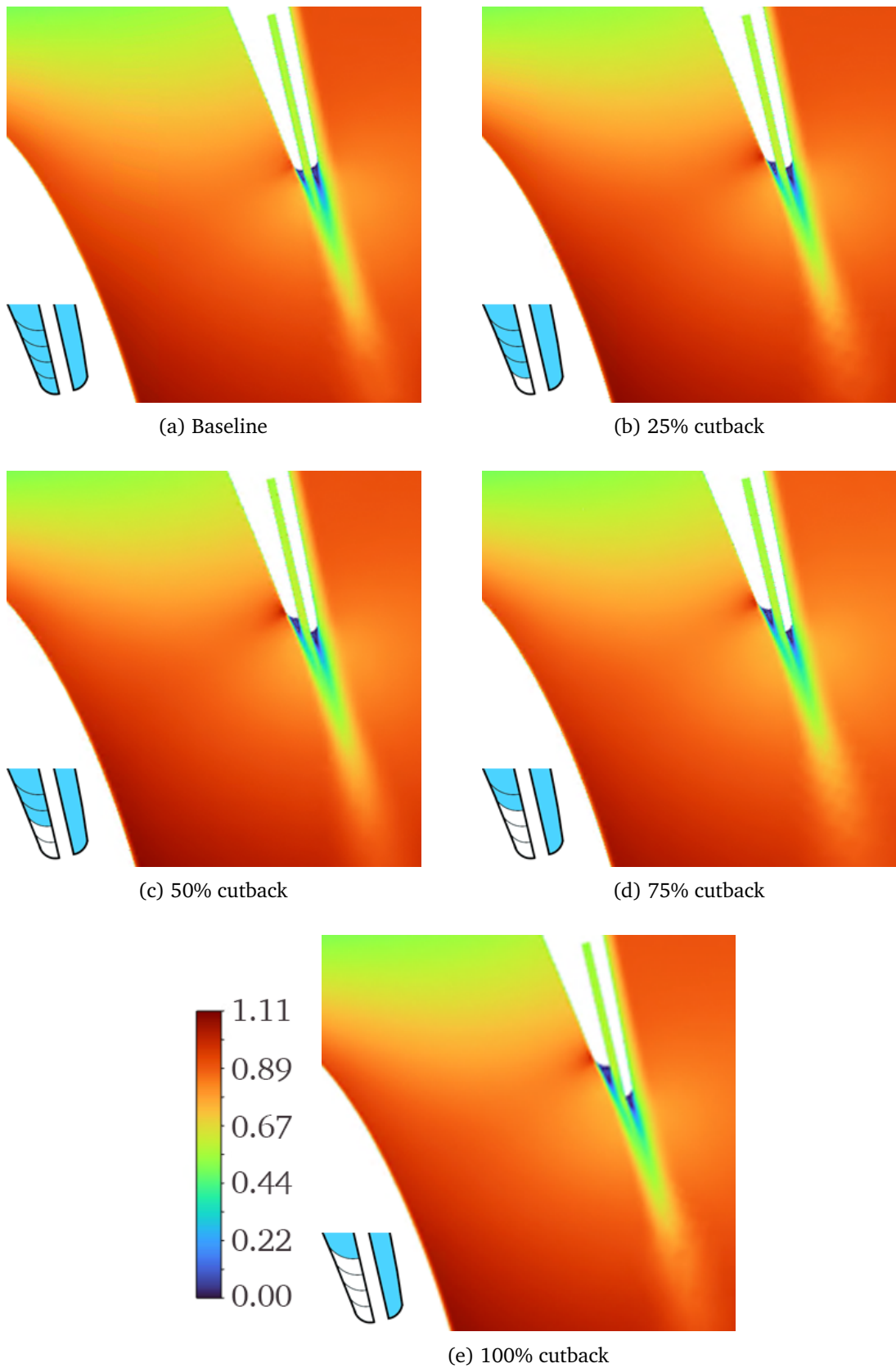


Figure 3.20: Effects of cutbacks on trailing edge aerodynamics for Trent 900 pressure-side cutback study at $\frac{p_{01}}{p_2} = 1.79$ (design)

Figure 3.20 shows that the trailing edge region aerodynamics remained fundamentally unchanged

in the case of incremental pressure-side cutbacks at the design pressure ratio. An exception to this was the presence of a region of accelerated flow adjacent to the area near the end of the pressure side where the vane surface has high convex curvature. This feature became more pronounced as cutbacks increased, suggesting that it contributed to the non-linear relationship between cutback amount and flow capacity delta at the design inverse pressure ratio.

Another significantly changing feature occurred directly downstream of this region, where the flow remained attached along part of the convex surface. The high-momentum mainstream is observed to turn towards the positive x -direction more as cutback increased, impinging on the low-momentum outer wake region. This resulted in reduced flow turning overall, which will be discussed subsequently. This downstream flow straightening corresponds to an expansion in the effective flow width downstream of the vane, a change which is likely a primary cause of the observed trend of capacity increasing sharply with smaller cutbacks. In the extreme, the transformation of outer wake area into mainstream area is limited by the momentum of the slow coolant flow, which prevents the mainstream from completely overwhelming the wake. This is likely the reason why both unchoked cases exhibited reduced sensitivity of capacity to cutbacks at larger cutback amounts.

Figure 3.21 plots trends of flow capacity change versus inverse pressure ratio at selected cutback amounts. The range of inverse pressure ratios includes the design value of 1.79.

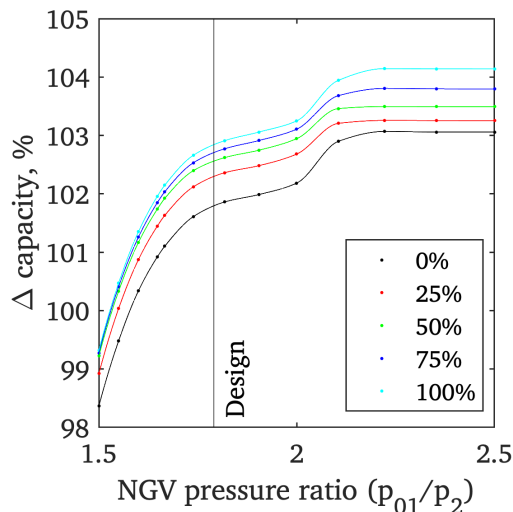


Figure 3.21: 2D capacity trends for various pressure-side cutback amounts

Figure 3.21 is in good agreement with Figure 3.19. The capacity delta produced by a 100% pressure-side cutback continuously increased with increasing inverse pressure ratio. It is concluded that, as inverse pressure ratio increased, more streamlines became choked, causing effects such as downstream flow straightening and expansion to have a reduced effect on flow capacity. When the flow was fully choked, capacity changes were almost directly proportional to the throat width changes that corresponded to the incremental cutbacks. This is complementary to the conclusions of Section 3.2, where capacity changes were primarily driven by effects other than a changing throat area, and were thus more sensitive at lower inverse pressure ratios rather than higher ones.

Capacity trends remained qualitatively similar for all cutback amounts. It is thus further concluded that the capacity trend shapes and onsets of choking were unaffected by pressure-side cutbacks, but remained a function of only inverse pressure ratio. This is likely due to the relevant geometric changes taking place downstream of the throat region. Both the conclusions of Section 3.2 and this section are complementary to the results of Chapter 2.

3.3.3 Effect on performance

Simulation data were also used to evaluate the aerodynamic penalties associated with the incremental cutbacks to the pressure side at the design inverse pressure ratio of 1.79. These penalties include the change to the NGV's ability to turn the flow by the correct angle, and the effect of the cutbacks on the NGV loss.

Velocity components at the domain outlet were surveyed and averaged over the length of the outlet. This resulted in a value for mean NGV turning angle for each incremental cutback. Figure 3.22 plots turning angle deviation in degrees versus pressure-side cutback amount.

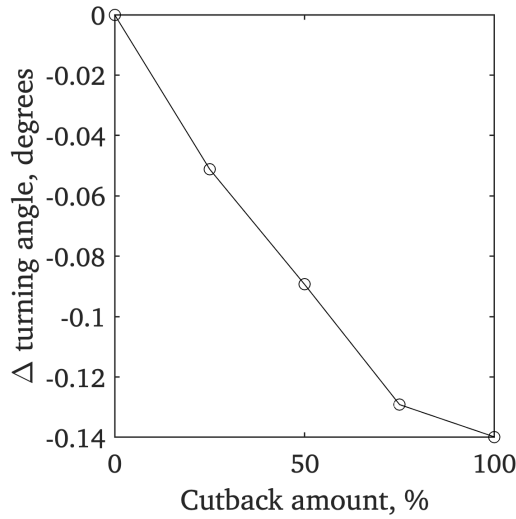


Figure 3.22: NGV turning angle delta as a function of pressure-side cutback amount at $\frac{p_{01}}{p_2} = 1.79$

Figure 3.22 shows that the NGV's ability to turn the flow was slightly reduced as cutbacks increased. Complete removal of the end-edge resulted in a turning angle reduction of 0.14 degrees. This is approximately half the sensitivity to end-edge cutbacks shown to be present in Section 3.2, which was 0.3 degrees. It is suggested that the correct end-edge length is more essential for proper flow turning than the position of the trailing edge's pressure side.

Overall flow turning angle was surveyed along the length of the domain outlet plane. Figure 3.23 plots this distribution of turning angles throughout the range of cutback amounts. On the outlet plane, 0→1 denotes travel in the negative y direction, which is the direction the flow turns. Stations 0 and 1 are labelled on the illustration of the computational domain in Chapter 2, Figure 2.3.

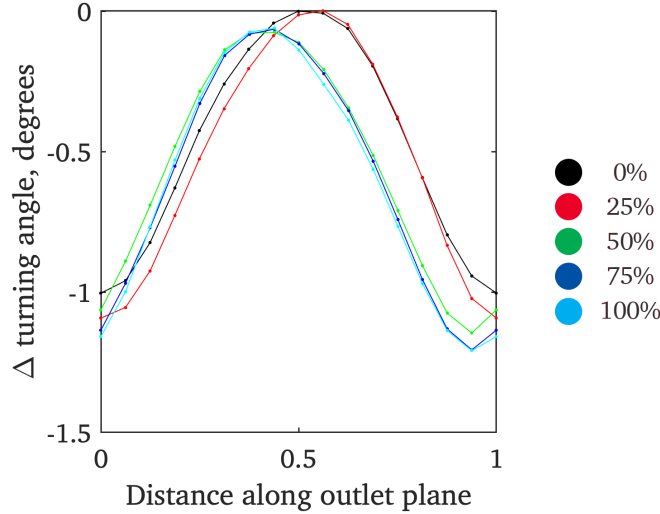


Figure 3.23: Outlet plane turning angle surveys for various pressure-side cutback amounts at $\frac{p_{01}}{p_2} = 1.79$

Figure 3.23 indicates that there is not an obvious pattern to describe the changes that occurred to the flow turning angle downstream of the NGV. Overall, the location of maximum turning was observed to move in the positive y direction. This is both intuitive given that material is being removed from the vane, and in agreement with the similar observation from Section 3.2. It is interesting to note that the first pressure-side cutback of 25% produced a small change in the location of maximum turning in the opposite direction to the general trend, although mean turning angle was slightly reduced even by this cutback amount. Subsequent cutbacks resulted in an apparent mode switch where the maximum turning location was shifted in the positive y direction but was only negligibly affected by changes to cutback size between 50% and 100%. This behaviour was likely related to the observed post-throat flow straightening at smaller cutback sizes. At larger cutback sizes this behaviour was limited by interaction between the mainstream and the slot coolant flow momentum, and by the presence of the potential field from the end-edge, which re-establishes flow turning.

Figure 3.24 plots loss as a function of pressure-side cutback amount at the design pressure ratio of 1.79, where total pressure loss and kinetic energy loss are defined as in Section 3.1. Total pressure values were surveyed at the domain outlet plane and averaged to produce the loss values.

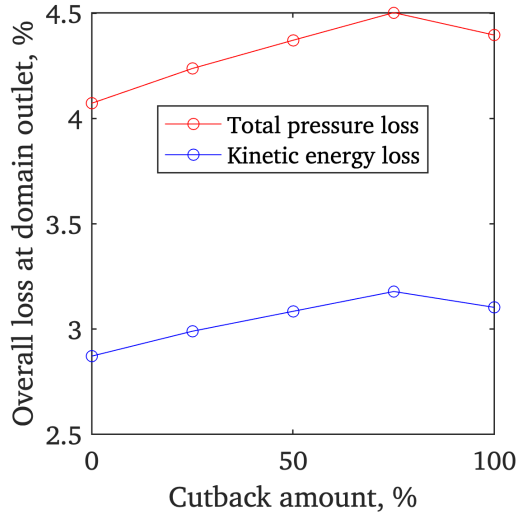


Figure 3.24: Loss as a function of pressure-side cutback amount at $\frac{p_{01}}{p_2} = 1.79$

Figure 3.24 shows that both types of loss initially increased with increasing cutbacks, but were decreasing at the final and largest cutback size. This is largely in agreement with the hypothesis that larger cutbacks produce larger wake areas which produce more loss, but the final data points suggest that a counteractive mechanism is also present and becomes dominant at the largest cutback size. This mechanism may involve the aforementioned impingement onto the pressure-side wake from the mainstream at the largest cutback size, reducing the area of this wake region and reversing the trend of increasing loss. Total pressure loss was observed to increase by approximately 0.32% over the range of cutbacks, and kinetic energy loss by approximately 0.23%.

Loss delta is plotted as a function of capacity delta in Figure 3.25. This plot covers the range of incremental cutbacks and is for the design inverse pressure ratio of 1.79.

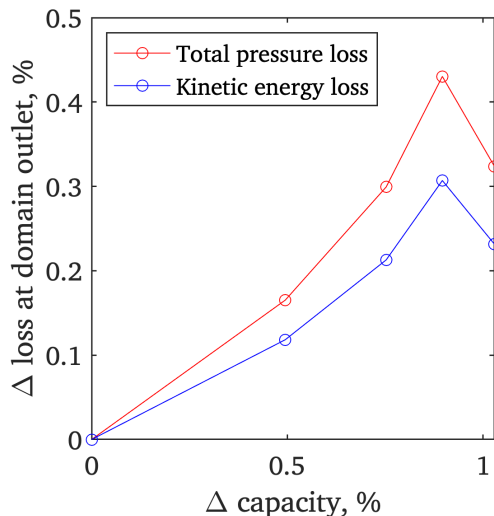


Figure 3.25: Loss delta as a function of capacity delta for pressure-side cutbacks at $PR = 1.79$

Figure 3.25 shows that, as the pressure side is incrementally removed, capacity and loss do not change in direct proportion to each other. Overall capacity sensitivity was greater than overall loss sensitivity by approximately a factor of two, which is similar to the equivalent result in Section 3.2.

At higher cutback amounts a relatively small increase in capacity corresponded to a sharp increase in loss by both definitions, except for the case of 100% cutback where loss was observed to decrease as discussed.

3.4 Chapter conclusions

Changes to the suction-side end-edge of the simulated NGV and changes to its pressure side cutback have both been shown to cause changes to the vane's flow capacity and aerodynamic performance.

Although capacity consistently increases when material is removed from either side of the trailing edge, the suction-side changes and the pressure-side changes are dominated by different mechanisms. Removal of suction-side end-edge material allowed for greater flow expansion downstream of the geometric throat, and consequently the flow capacity was more affected at unchoked pressure ratios. In contrast, the pressure-side cutbacks directly affected the width and location of the geometric throat, and the flow capacity was more affected at more choked pressure ratios where capacity is wholly set by the conditions on the sonic line as shown in Chapter 2.

Aerodynamic performance evaluations have included total pressure loss, kinetic energy loss, and flow turning angle deviation. All of these are shown to be affected by changes to either side of the trailing edge, although all were less severely affected by the pressure-side changes than by the suction-side ones. In all cases, loss increases are shown to result from increases in wake area caused by earlier boundary layer separation and improper shaping of the flow by the altered trailing edge. Improper flow shaping is also shown to cause the flow to excessively expand downstream of the NGV and experience improper turning. Turning errors are found to follow a simple trend in the case of suction-side changes, where end-edge material removal causes an incremental reduction in the vane's turning without fundamentally changing the wake profile. Pressure-side changes are shown to cause an interaction between the mainstream and the slot coolant flow, leading to a relationship between pressure-side cutbacks and turning angle surveys which is more difficult to categorise.

Chapter 4

Film cooling

Chapter 2 has discussed how variations in the nozzle guide vane's overall cast shape affect flow capacity and performance, developing analytical techniques to draw conclusions about the relevance of throat width versus other factors at different pressure ratios. Chapter 3 has focused these analytical techniques on the NGV trailing edge, whose proximity to the throat region causes it to significantly affect capacity if its geometry is subject to small changes. This chapter will complete the present study's evaluation of near-throat variations by considering the effects of film coolant injection on the NGV suction side.

If a film cooling row is required on this part of the vane, small variations in the row's placement will cause the film coolant to be injected at various locations throughout the throat region. At choking pressure ratios, injection locations immediately upstream of the sonic line are expected to cause distinctly different effects compared to injection locations downstream of the sonic line. At all pressure ratios, varying the film coolant injection location is expected to cause variations in capacity and performance. This is due to the exchange of momentum between film coolant and mainstream, and due to the resulting variation in downstream boundary layer thickness which directly affects the effective throat width.

4.1 Sensitivity of capacity to cooling holes on the leading suction side

This section will consider the effects of varying the location of a single row of film cooling holes on the suction side of an otherwise uncooled nozzle guide vane. The introduction of film coolant in this region is shown to affect the NGV flow capacity, and this effect is shown to be sensitive to the precise location of the film cooling hole row. This section uses the Rolls-Royce Trent XWB 84K nozzle guide vane as its baseline geometry. This has been selected because it represents one of the latest iterations of contemporary large civil aero engines, introduced into service in 2015 to power the Airbus A350 XWB. Successive generations of aero engines such as the Trent XWB 96K have used increasingly high pressure ratios and combustor outlet temperatures, and thus the latest engine design is considered to be the most representative of designs most likely to require additional film cooling in future.

4.1.1 Geometry, mesh, and boundary conditions

If a film cooling row is to be modelled using 2-dimensional CFD, several considerations must be made to ensure the simulation is representative of real engine conditions. These considerations fall into 2 categories, namely the correct setting of boundary conditions at the coolant inlet, and the mitigation of 3-dimensional flow phenomena that affect coolant mixing but are not captured by 2-dimensional simulations.

The coolant inlet boundary exists to model the network of passageways that feeds compressor bleed air to the film cooling holes in a real engine. The present study represents this as a small plenum connected to the coolant hole. The coolant hole is specified as a narrow rectangular passage of engine-representative diameter, with no-slip walls. Total pressure is specified on the coolant plenum walls. An example of a 2D CFD domain for a single cooling row and its plenum is shown in Figure 4.1.

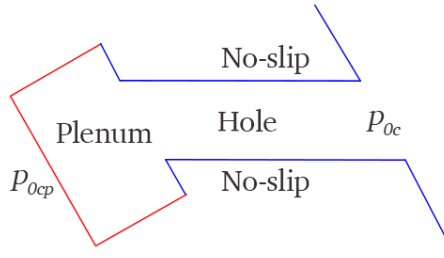


Figure 4.1: Computational domain and boundaries for a film cooling hole and plenum

The present study aims to simulate an engine-representative ratio of coolant-to-mainstream mass flow rate. Although it is optional to specify a desired mass flow rate on an inlet boundary in CFD, this is not a realistic simulation of the physics of a nozzle guide vane, where the designer has instead specified a total pressure within each film coolant plenum. The coolant flow through the plenum and hole is then subject to a degree of total pressure loss. The resulting mass flow rate from the film cooling hole is related to the total pressure and temperature at the hole exit p_{0c} and T_{0c} , the local mainstream static pressure p_m , and the hole cross-sectional area A_h by an adapted form of equation 1.12, as

$$\dot{m}_c = \frac{p_{0c}}{\sqrt{T_{0c}}} A_h \sqrt{\frac{\gamma}{R}} \left(\frac{p_m}{p_{0c}} \right)^{\frac{1}{\gamma}} \sqrt{\left(\frac{2}{\gamma - 1} \right) \left[1 - \left(\frac{p_m}{p_{0c}} \right)^{\frac{\gamma-1}{\gamma}} \right]} \quad (4.1)$$

For a desired value of \dot{m}_c and a value of p_m calculated at a benchmark cooling hole location, it is thus possible to compute a required value of p_{0c} . This may be achieved iteratively by rearranging equation 4.1 as

$$x_n = p_m \left[1 - \frac{R(\gamma - 1)}{2\gamma} T_{0c} \left(\frac{\dot{m}_c x_{n-1}^{\frac{1-\gamma}{\gamma}}}{A_h p_w^{\frac{1}{\gamma}}} \right)^2 \right]^{\frac{\gamma}{1-\gamma}} \quad (4.2)$$

where $x = p_{0c}$. T_{0c} is assumed to be 300K as the present study assumes adiabatic conditions. Significant total pressure loss is assumed to occur between the coolant plenum and the point where the coolant exits the hole to mix with the mainstream. This loss may be quantified in a form similar to the general total pressure loss coefficient in equation 3.1, as

$$\zeta_c = \frac{p_{0cp} - p_{0c}}{p_{0cp} - p_m} \quad (4.3)$$

Although typical values for p_{0cp} and ζ_c may be referenced from the literature, the present study sought to report values accurate for the case of 2-dimensional CFD where loss mechanisms are unlike those present in either a real coolant plenum or in 3D CFD. A CFD solution was converged using the same benchmark cooling hole location as was used to report the benchmark p_m for equation 4.2. The coolant plenum was, in this special case, specified with the desired coolant mass flow rate. The reported value for p_{0cp} (area-averaged across the plenum inlet boundary) was used as the benchmark value for all subsequent simulations, and was used along with the reported value for p_{0c} (area averaged across the plenum hole exit) to evaluate ζ_c .

A series of 2D CFD simulations were then performed with a single cooling hole at a range of locations throughout the nozzle guide vane throat region. The baseline geometry is the Rolls-Royce Trent XWB 84K nozzle guide vane. A 2D vane section was produced using the process illustrated in Figure 2.2. The overall computational domain was produced as in Figure 2.3. The NGV trailing edge was smoothly rounded as this section of study is not concerned with trailing edge effects. The NGV surface was modified to include the cooling hole and plenum with its total pressure inlet boundary condition described above. Matlab was used to parametrically generate 7 geometries by moving the single cooling hole between 0% and 100% of its range of travel in increments of approximately 16%, although spacing of simulated hole locations was closer in the throat region of the nozzle. The boundary conditions used for all simulations are listed in Table 4.1. The range of hole locations is illustrated in Figure 4.2.

Simulations were performed at the design inverse pressure ratio of 1.65 but not at a fully choked inverse pressure ratio. This decision was made because the majority of the range of hole locations lie downstream of the nozzle's sonic line. In accordance with the other findings of this study, these locations are expected to have minimal effect on the NGV capacity.

Table 4.1: Boundary conditions for suction-side cooling hole position study

Parameter	Value
NGV series	Rolls-Royce Trent XWB 84K
NGV turning (degrees)	73.97
NGV throat width (m)	1.25×10^{-2}
Design inverse pressure ratio	1.65
Inlet total pressure (Pa)	4.33×10^6
Inlet total temperature (K)	300
Outlet static pressure (Pa)	2.63×10^6
Outlet static temperature (Pa)	300
Benchmark coolant mass flow rate	1.00% of mainstream
Film coolant loss coefficient ζ_c	0.8
Coolant plenum total pressure p_{0cp}	79.91% of mainstream
Solver type	Density-based
Cell count	40,000

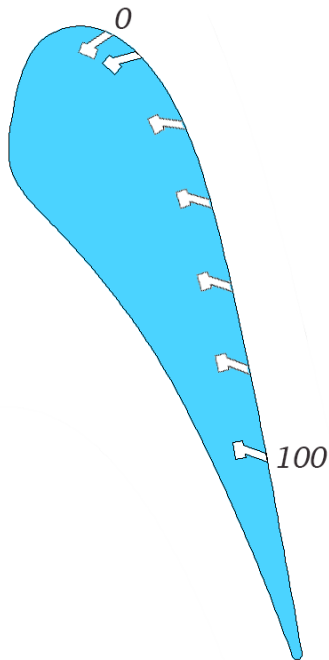
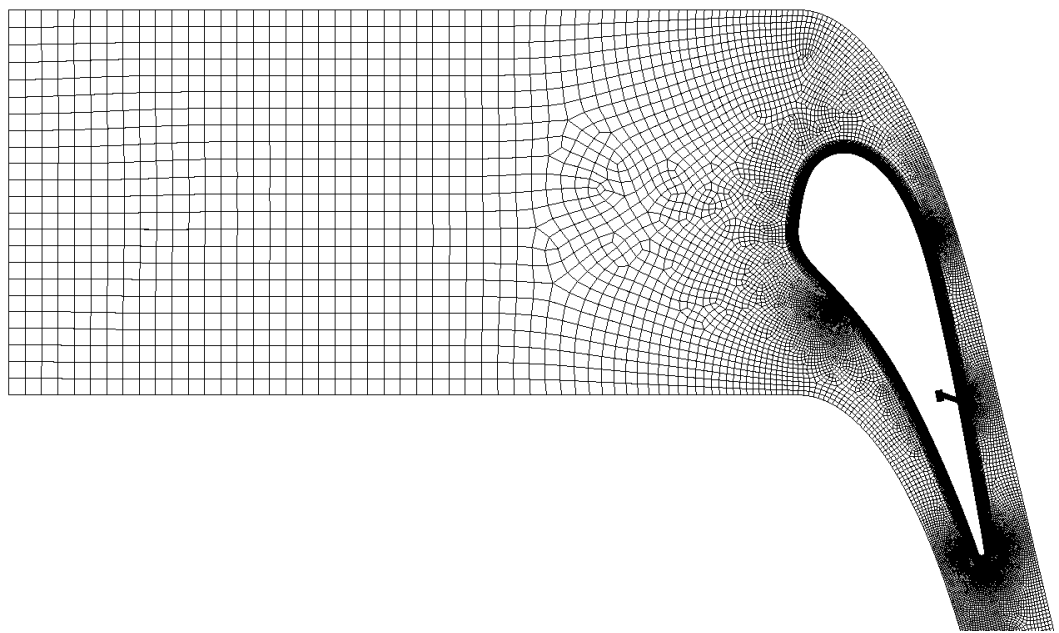
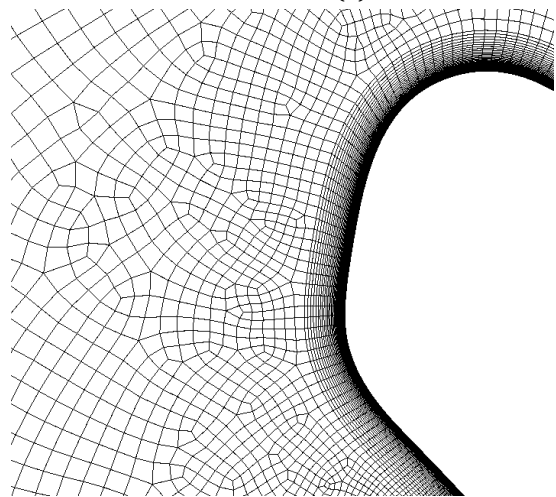


Figure 4.2: Range of locations for a single suction-side film cooling hole on a Trent XWB NGV

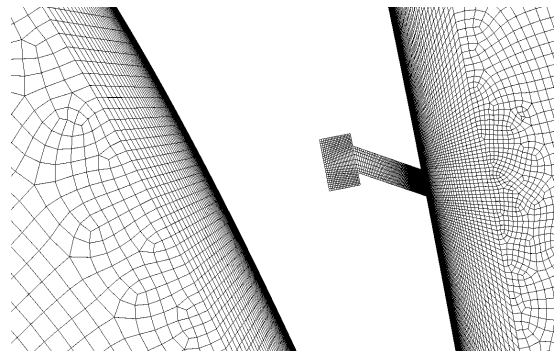
Figure 4.2 depicts a range of geometries which allows the introduction of film coolant at various locations both upstream and downstream of the NGV geometric throat (and its sonic line in the case of fully choked flow). As the cooling hole and plenum consist of 2 rectangles, each was assigned a structured quadrilateral mesh that could be matched with a structured boundary layer mesh of the same design as that depicted in Figure 2.5a. Beyond this, an unstructured mesh was created to the same design as that depicted in Figure 2.4. Details of the resulting mesh are shown in Figure 4.3 for a case where the single cooling hole is near the downstream end of its range of locations.



(a) XWB mesh for NGV and upstream domain



(b) XWB mesh for leading edge



(c) XWB mesh for cooling hole and plenum

Figure 4.3: Details of mesh for XWB single cooling hole study

4.1.2 Effect on capacity

Figures 4.4 and 4.5 show contours of Mach number in the region of the nozzle guide vane for the described study. Inverse pressure ratio is 1.65, the design cruise condition.

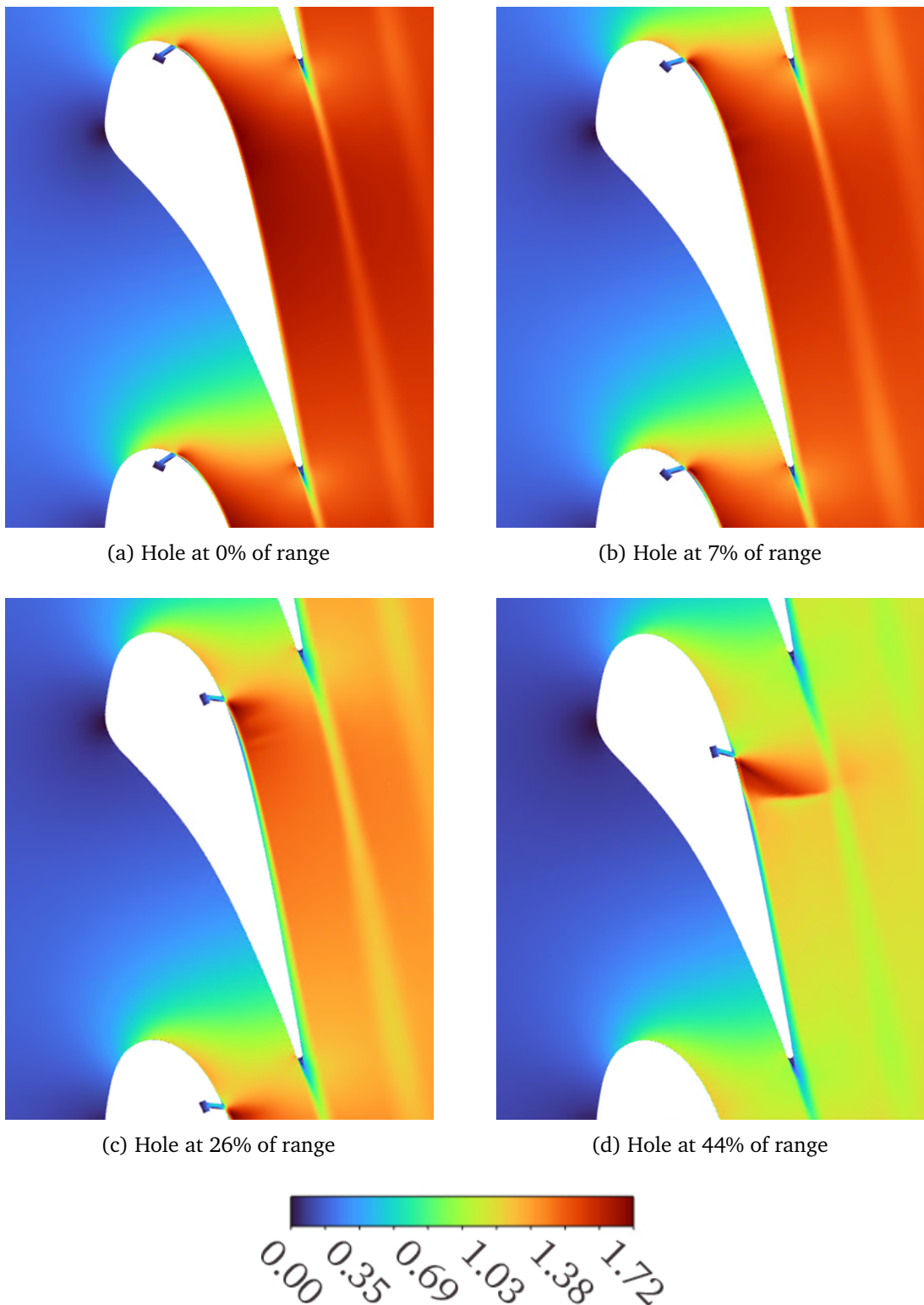


Figure 4.4: Effects of cooling hole location on Mach contours for Trent XWB film cooling study at $\frac{p_{01}}{p_2} = 1.65$

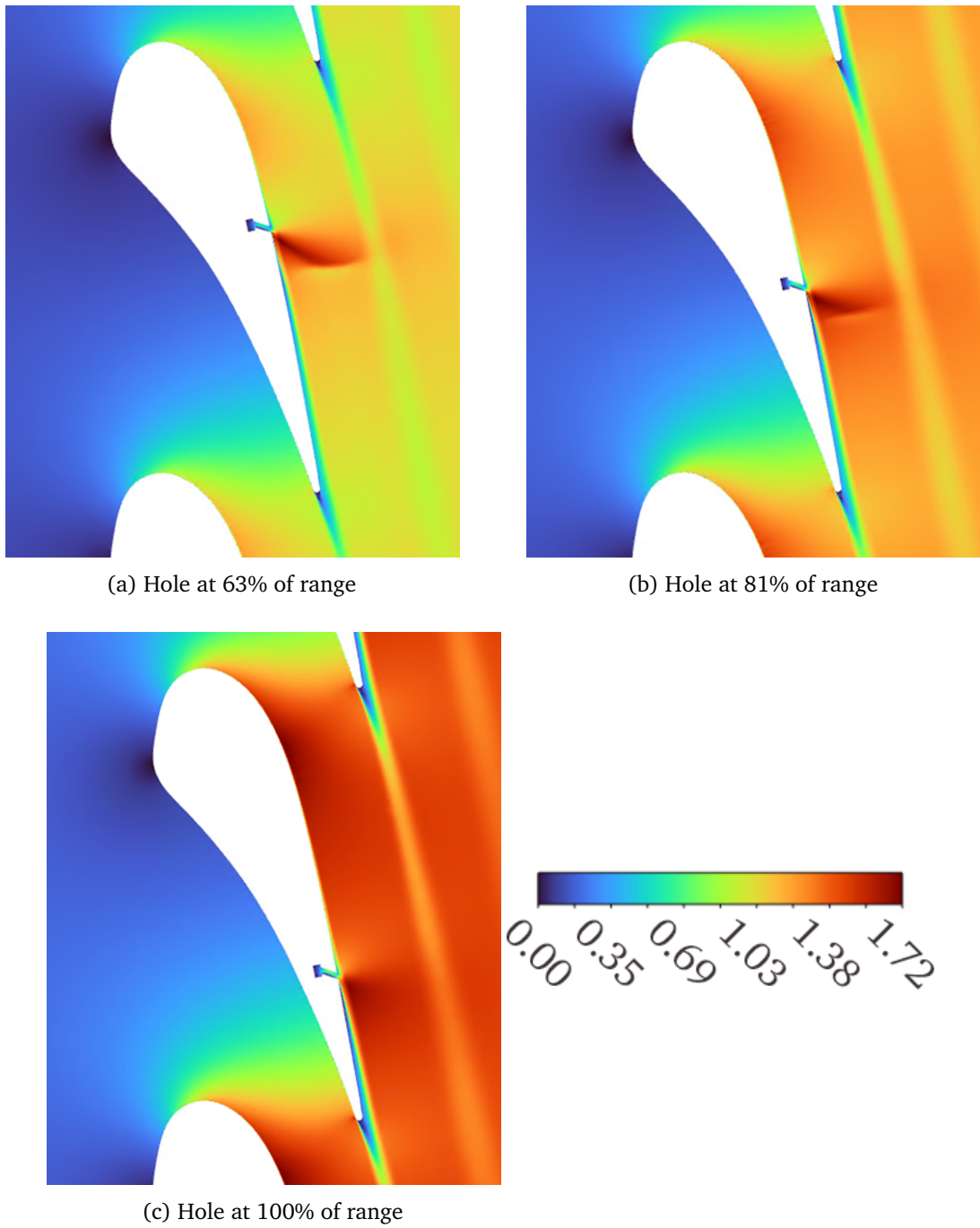


Figure 4.5: Effects of cooling hole location on Mach contours for Trent XWB film cooling study at $\frac{p_{01}}{p_2} = 1.65$

Figures 4.4 and 4.5 illustrate the presence of transonic flow phenomena that varied significantly with the variations to the location of film coolant injection. Injection locations upstream and far downstream of the throat region caused localised flow acceleration as the potential field of the coolant jet caused a narrowing of the effective throat area. At injection locations immediately downstream of the throat, where the mainstream flow velocity was greatest, this effect was significantly stronger. Here the local acceleration resulted in regions of supersonic flow within the mainstream, followed by deceleration through a shock attached to the suction side of the nozzle guide vane.

In all cases, the suction side boundary layer thickness increased immediately downstream of the

film cooling hole, due to the mainstream flow being displaced by the momentum of the coolant jet in the direction perpendicular to the NGV surface. In the cases with the hole at 0% and 7% of the range of travel, where the injection location was upstream of the geometric throat, this increase in boundary layer thickness amounted to a local bubble after which the boundary layer became thinner again and experienced conventional growth further downstream. In the case with the hole at 26% of the range of travel, the coolant injection appeared to initiate a growth of the boundary layer which began immediately downstream of the hole and continued throughout the suction side of the NGV, resulting in a distinctly thicker boundary layer at the suction side trailing edge compared to the cases of pre-throat coolant injection.

In the cases with the hole at 44% and 63% of the range of travel, where the coolant-induced acceleration and shock were strongest, the coolant-induced boundary layer growth appeared to be delayed until the point of shock attachment on the NGV suction side. Downstream of this, an uninterrupted boundary layer growth again resulted in a thick boundary layer at the suction side trailing edge. In the cases with the hole at 81% and 100% of the range of travel, boundary layer growth was reminiscent of the case of 26%, initiating immediately downstream of the film cooling hole despite the presence of supersonic regions and shocks. All of these observations suggest that shock loss is an important factor in evaluating the performance effects of the cooling hole location. This will be discussed subsequently.

Figure 4.6 plots the percentage change in the NGV flow capacity as a function of the cooling hole location. For this analysis, two definitions of capacity are provided. The first, Γ_{in} , is defined as

$$\Gamma_{in} = \frac{\sqrt{T_{01}}}{p_{01}} \dot{m} \quad (4.4)$$

where T_{01} and p_{01} are the upstream total conditions and \dot{m} is the mainstream mass flow rate measured at the domain inlet. The second definition, Γ_{out} , represents the capacity of the flow leaving the domain, and is defined as

$$\Gamma_{out} = \frac{\sqrt{T_{01}}}{p_{01}} \dot{m} + \frac{\sqrt{T_{0c}}}{p_{0c}} \dot{m}_c \quad (4.5)$$

where T_{0c} and p_{0c} are the upstream total conditions and \dot{m}_c is the coolant mass flow rate which may vary with injection location as the coolant plenum is specified by total pressure instead of mass flow rate.

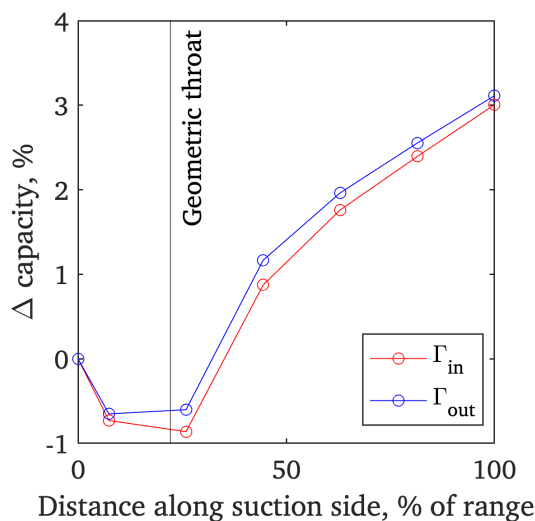


Figure 4.6: Total capacity percentage delta as a function of single cooling hole position

Figure 4.6 shows a general trend of flow capacity increasing as the film coolant is injected. The maximum range of Γ_{in} was 3.87% over the range of hole locations, and the maximum range of Γ_{out} was 3.76%. This trend is uniformly true for the cases where coolant is injected downstream of the geometric throat. It is hypothesised that this capacity increase is primarily driven by the introduction of the coolant into regions of progressively lower mainstream flow velocity as the hole location moves downstream and away from the throat region. This decrease in mainstream flow velocity is observable in Figures 4.4 and 4.5 and is to be expected of unchoked flow downstream of the throat of a nozzle guide vane. Assuming that, in general, film coolant affects NGV capacity via the exchange of momentum between the fast mainstream and the slower coolant, it is concluded that this deficit to mainstream flow momentum is less severe as the coolant is injected into slower regions further downstream.

This hypothesis is supported by the capacity predictions for the cases where coolant is injected upstream of, or very near, the NGV geometric throat. Compared to the furthest location upstream, the 2 subsequent downstream locations resulted in a deficit to flow capacity which was most severe in the region local to the throat. Here the mainstream flow velocity was highest and thus the coolant injection would be expected to cause the greatest deficit to mainstream momentum and thus mass flow rate. This hypothesis may be further tested by considering the isentropic Mach number on the NGV surface, which may be defined as

$$M_{isent} = \sqrt{\frac{2}{\gamma - 1} \left[\left(\frac{p_{01}}{p_m} \right)^{\frac{\gamma-1}{\gamma}} - 1 \right]} \quad (4.6)$$

Figure 4.7 plots the percentage change in the NGV flow capacity as a function of the surface isentropic Mach number at each cooling hole location. Data points are connected to convey the sequence of incremental changes to the hole location.

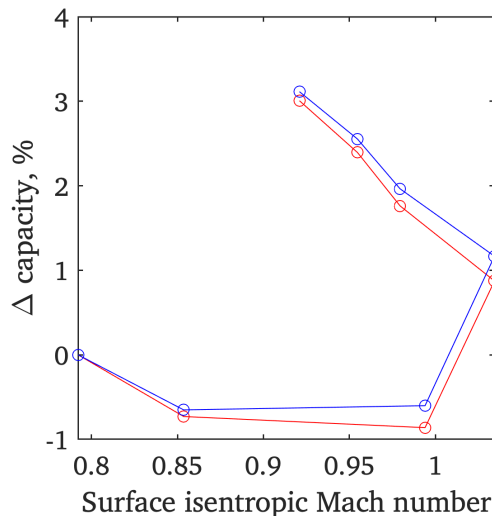


Figure 4.7: Total capacity percentage delta as a function of surface isentropic Mach number

Figure 4.7 shows a relationship between surface isentropic Mach number and flow capacity which is in agreement with the prior discussion for cases downstream of the geometric throat, as capacity decreased as the coolant was injected into locations having a higher Mach number. The 3 data points furthest upstream are less clearly interpretable. A trend of capacity decreasing with local Mach number was arguably present, however these data were not in alignment with those downstream

of the throat. This suggests that a consideration of the local flow velocity or Mach number does not entirely explain the observed relationship between hole location and capacity.

We may also examine the variation in the capacity of the coolant itself as it is injected at various locations at a constant plenum total pressure. The coolant capacity is defined as

$$\Gamma_c = \frac{\sqrt{T_{0c}} \dot{m}_c}{p_{0c}} \quad (4.7)$$

Figure 4.8 plots the coolant capacity as a function of the cooling hole location.

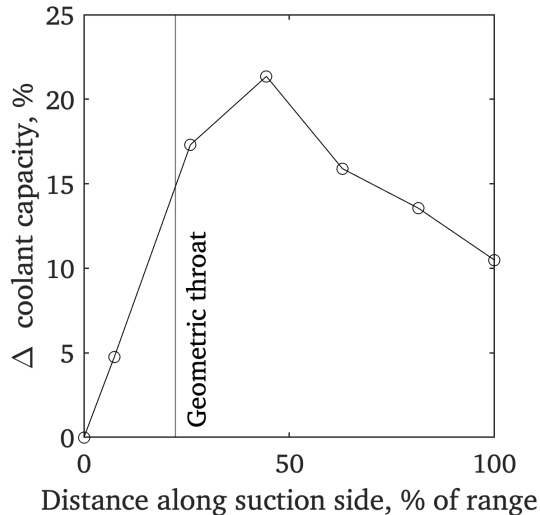


Figure 4.8: Coolant capacity percentage delta as a function of single cooling hole position

Figure 4.8 shows that the coolant capacity varied significantly with the hole location, with the maximum range being approximately 21.35%. This variation is hypothesised to be the result of different hole locations causing the coolant to be injected into regions of different static pressure, with correspondingly different pressure ratios as defined in equation 4.2. A static pressure coefficient may be defined using the NGV surface static pressure at each hole location as

$$C_p = \frac{p_m - p_m(\min)}{p_m(\max) - p_m(\min)} \quad (4.8)$$

Figure 4.9 plots the coolant capacity as a function of the NGV surface static pressure coefficient.

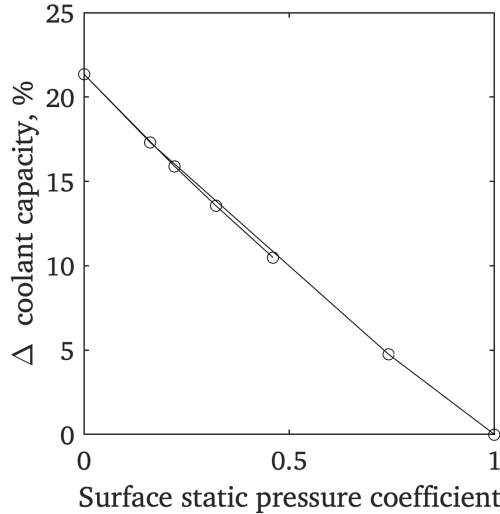


Figure 4.9: Coolant capacity percentage delta as a function of single cooling hole position

Figure 4.9 illustrates that the coolant capacity is highly dependent on the local static pressure at the point of injection. It is concluded that the coolant plenum is well-modelled as a supersonic nozzle and that the ratio of $\frac{p_{oc}}{p_m}$ is a good predictor of the coolant mass flow rate for a given plenum static pressure and engine-representative value of ζ_c .

4.1.3 Effect on performance

Shock loss has been hypothesised to be a significant influence on the aerodynamic performance of the present configuration at different cooling hole locations. Figure 4.10 plots loss (as defined by equation 3.1) as a function of single cooling hole position.

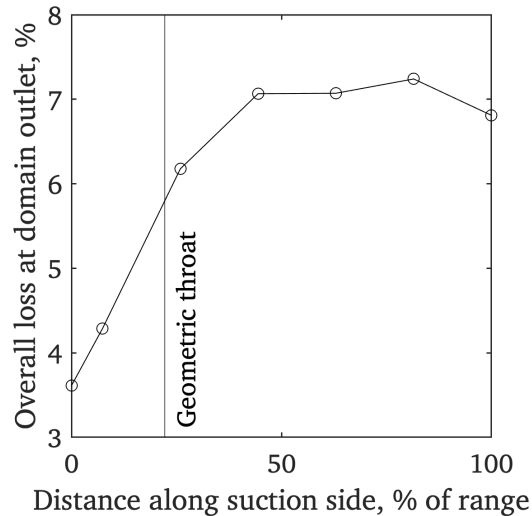


Figure 4.10: Loss as a function of single cooling hole position

The trend exhibited in Figure 4.10 is in good agreement with the prior discussion of Figures 4.4 and 4.5 which suggests that the degree of aerodynamic loss incurred will correlate strongly with

the strength of shocks precipitated by the injection of film coolant. The Mach contours show the increasing appearance of shocks as the coolant is introduced further downstream, with shocks most apparent when the coolant hole is at 44%, 63%, and 81% of its range of positions. Correspondingly these positions resulted in the greatest amount of total pressure loss. It is concluded that shock loss is the primary loss mechanism driving the observed trend.

Bibliography

- [1] A. Guiffre' and M. Pini, "Design guidelines for axial turbines operating with non-ideal compressible flows," *Proceedings of ASME Turbo Expo*, 2020.
- [2] D. Thirumurthy, J. C. C. Coca, and K. Suraweera, "Capacity matching of aeroderivative gas generator with free power turbine: Challenges, uncertainties, and opportunities," *Proceedings of ASME Turbo Expo*, 2019.
- [3] T. Hall, "Trent 900 CFD investigation of HPNGV capacity sensitivity to trailing edge geometry," Tech. Rep. DNS 170140, Rolls-Royce plc, Gipsy Patch Lane, Filton, Bristol, March 2011.
- [4] G. Zamboni, "HYDRA CFD of the trent 900 EP1 turbine high pressure nozzle guide vane: analysis of the trailing edge slot geometry influence on capacity predictions using gom scanned data," Tech. Rep. DNS 181981, Rolls-Royce plc, Gipsy Patch Lane, Filton, Bristol, July 2012.
- [5] J. Nikuradse, "Laws of flow in rough pipes," *VDI Verlag research booklet; "supplement to Research in the field of engineering"*, vol. 361, no. B4, 1933.
- [6] H. Schlichting, *Boundary Layer Theory*. New York, NY, USA: McGraw-Hill, 1979.
- [7] S. M. Salim and S.-C. Cheah, "Wall $y+$ strategy for dealing with wall-bounded turbulent flows," *Proceedings of the International MultiConference of Engineers and Computer Scientists*, vol. II, 2009.
- [8] ANSYS Inc., "Overview of FMG initialization." <https://www.afs.enea.it/project/neptunius/docs/fluent/html/th/node388.htm>, 2009. Accessed: 2021/06/23.
- [9] D. B. da Trindade, P. Bugala, and D. Simone, "Review of loss models for high pressure turbines," *Journal of KONES Powertrain and Transport*, vol. 25, no. 2, pp. 37–44, 2018.
- [10] P. W. Giel, V. Shyam, P. Juangphanich, and J. P. Clark, "Effects of trailing edge thickness and blade loading distribution on the aerodynamic performance of simulated cmc turbine blades," *Proceedings of ASME Turbo Expo*, 2020.
- [11] J. Gau, M. Wei, W. Fu, Q. Zheng, and G. Yue, "Experimental and numerical investigations of trailing edge injection in a transonic turbine cascade," *Elsevier Journal of Aerospace Science and Technology*, vol. 92, pp. 258–268, 2019.
- [12] R. Saha, J. Fridh, and T. H. Fransson, "Shower head and trailing edge cooling influence on transonic vane aero performance," *Proceedings of ASME Turbo Expo*, 2014.
- [13] M. Deckers and J. D. Denton, "The aerodynamics of trailing-edge-cooled transonic turbine blades: Part 1 - experimental approach," *Proceedings of ASME Turbo Expo*, 1997.
- [14] S. M. Jones, W. J. Haller, and M. T. Tong, "An n+3 technology level reference propulsion system," *NASA technical memorandum*, 2017.